Turbulence statistics and transport in compressible mixing driven by spherical implosions with narrowband and broadband initial perturbations

Moutassem El Rafei *
School of Aerospace, Mechanical and Mechatronic Engineering, University of Sydney, Sydney, New South Wales 2006, Australia

Ben Thornber
School of Mechanical and Aerospace Engineering, Queen's University Belfast, Belfast BT9 5AH, Northern Ireland, United Kingdom

(Received 28 October 2022; accepted 31 January 2024; published 4 March 2024)

Compressible turbulent mixing evolving from Richtmyer-Meshkov and Rayleigh-Taylor instabilities and Bell-Plesset effects has been investigated using high-resolution implicit large eddy simulations of fundamental spherical implosion problems. Broadband (BB) and narrowband (NB) initial perturbations consisting of multimode cosine perturbations are considered at a high Atwood number ($A_t = 0.9$) corresponding to a density ratio of 20. This research examines the turbulent transport and budgets of turbulent kinetic energy, turbulent mass flux, and density self-correlation, and the balance of the terms in the transport equations is used to approximate the numerical discretization effect on the derived equations. Strong non-Boussinesq effects and asymmetries were observed in the distribution of the anisotropy terms and budgets within the mixing layer. The production and destruction terms dominate the late stages of the mixing process in all the equations compared to the other transport terms. The BB layer showed higher levels of density self-correlation compared to the NB case, which showed larger destruction levels relative to the state of the layer. Higher levels of turbulent mass flux and turbulent kinetic energy (e.g., larger potential to kinetic energy conversion rates) were observed in the BB case due to the longer-wavelength perturbations in the BB layer that dominate the growth at late times. The numerical discretization terms implicitly modeling the effect of the unresolved scales contribute to both diffusion and dissipation and the current study shows that their effect may be both examined indirectly through residuals and quantified directly through observed destruction.

DOI: 10.1103/PhysRevFluids.9.034501

I. INTRODUCTION

The Rayleigh-Taylor instability (RTI) [1,2] occurs at the perturbed interface between a light fluid and heavy fluid, where the light fluid is accelerated into a heavy fluid [3]. The acceleration of the fluids into one another at the perturbed interface and the mismatch in density and pressure gradients cause the generation of baroclinic vorticity that starts the mechanism of Rayleigh-Taylor (RT) growth. One of the main applications where RTI is a major performance degradation factor is inertial confinement fusion (ICF) (see Refs. [4–9]). RTI appears in the process of generating fusion using ICF due to the compression of the fuel which resists the implosion of the shell of the capsule.

*moutassem.elrafei@sydney.edu.au

This induces a deceleration of the interface which gives rise to Rayleigh-Taylor instability [10]. As a result, the imploding motion loses its symmetry and deviates from spherical.

The Richtmyer-Meshkov instability (RMI) [11,12] is considered the impulsive counterpart of the RTI. It is generated by a shock wave (through which the flow properties such as density, pressure, temperature, and velocity change discontinuously) passing through the perturbed interface between a heavy fluid and a light fluid and causing the deposition of baroclinic vorticity due to a mismatch of pressure and density gradients. Unlike RTI, RMI occurs whether the acceleration is applied in the direction from the heavy to the light fluid or the inverse. The study of RMI is quite important in many applications of mixing, such as supersonic combustion in rotating detonation engines (RDEs) and scramjets, where shock waves induce RMI growth that results in a better fuel and oxidizer mixing and hence more efficient combustion [13]. Another example where RMI plays an important role is the ICF process where compression of an ICF capsule typically involves multiple shocks, each of which causes an impulsive acceleration and modifies the growth rate of the instability. RMI and RTI also play an important role in many other research areas such as supernova explosions [14–18], premixed combustion [19,20], and interaction between shock waves and premixed flames [21–23]. The reader is referred to the comprehensive reviews in Refs. [24–27] for more details and literature on RTIs and RMIs.

The perturbations grow initially in a linear fashion and then transition to a nonlinear regime where the perturbation amplitude is comparable to the wavelength (typically $a > 0.1\lambda$). In this regime, using linear theory to model the growth of the modes is not valid and modeling techniques able to solve for the nonlinear growth are required. The layer continues to evolve in time, develops roll-ups and secondary instabilities, and transitions to turbulence. Eventually, the layer may transition to a fully developed turbulent regime characterized by a self-similar behavior where the integral quantities reach self-similar values. Thus, it is quite important to understand the development of turbulence, mixing, and turbulent transport in the mixing layer. For that purpose, different computational techniques have been used for the understanding of the turbulent mixing process, such as direct numerical simulation (DNS), large eddy simulation (LES), and Reynolds-averaged Navier-Stokes (RANS) models. In addition to that, single-mode and multimode models (see, for example, Refs. [28–35]) have been developed to predict the linear and nonlinear growth perturbations using simple ordinary differential equations. The reader is also referred to Refs. [36–45] for more recent numerical studies on RMI and RTI turbulent mixing.

The limitation in computational power and the challenging very high Reynolds number configurations in RMI- and RTI-induced turbulent flows make the use of mixed models necessary to account for turbulent effects in variable-density flows where complex additional physics are involved (reactions, conduction, radiation, etc.) [25]. The RANS approach is one of the most popular models that are used to solve for the evolution of statistical turbulent quantities due to the reduction in computational time it offers to achieve convergence compared to LES and DNS approaches. All the turbulent length scales are modeled in the RANS approach using turbulence models that approximate the effect of turbulence on the mean flow quantities.

A variety of closure models for RANS approaches can be used for the simulations of turbulent mixing and these models differ principally by the number of transport equations that are added to the mean equations to close the higher-order correlations. The K-L [46–48] and K-ϵ [49] are popular two-equation models that are used for turbulent mixing applications. A transport equation of the specific turbulent kinetic energy K is considered along with a second transport equation for the turbulent length scale L (in the K-L model) and the dissipation rate ϵ (in the K-ϵ model) for the closure of the system of equations. Two-equation models have been used in many examples of variable-density flows such as the prediction of astrophysical phenomena [50], the estimation of mixing layer widths and statistics in ICF targets [51], two-dimensional (2D) compressible turbulent mixing flows [52], and constant- and variable-acceleration Rayleigh-Taylor mixing [53]. A downside of these models is that they are isotropic; however, RMI and RTI turbulent flows are inhomogeneous and anisotropic [54]. Moreover, careful attention should be taken while initializing the turbulent flow field variables since some of these models

assume that the flow is starting from a fully turbulent state and do not consider the transitional regime [25].

The turbulence transport model derived by Besnard, Harlow, and Rauenzahn (BHR model) [55] is used for variable-density flows and can incorporate the transitional regime of the mixing process. The BHR model, in its original form, is based on a Favre-averaged decomposition and includes transport equations for the Reynolds stresses, turbulent kinetic energy, density self-correlation, and turbulent mass flux. A detailed derivation of the BHR model equations and the different closure assumptions can be found in Ref. [55] and Refs. [56,57], respectively. Several variants of the BHR model have been developed for the prediction of the turbulent mixing process. They differ in the transport equations that are considered and the method of modeling the terms included in the evolution equations [56,57]. The reader is also referred to Refs. [58] and [59] for more recent efforts on RANS approaches and closure models in variable-density mixing applications.

Turbulence budgets and turbulence transport in RM and RT flows was the subject of investigation of several previous experimental and numerical studies (see Refs. [60–71]). These studies investigated asymmetries and non-Boussinesq effects in compressible turbulent mixing and quantified the importance of the budget terms and closure models in transport equations. In particular, the study of Livescu *et al.* [66] presented quantitative measurements of the budgets of each term in the transport equations using high-resolution DNS data to investigate the physics of RT variable-density (VD) flows and non-Boussinesq effects, to explore the applicability of the gradient diffusion hypothesis as a closure to the terms in the transport equation, and to provide a database to validate turbulence models. The most recent study by Wong *et al.* [45] presented a very detailed study of turbulent budgets for the planar RMI with reshock using very near DNS resolution and examined the impact of filtering on the budgets.

The work presented in this paper investigates temporal and spatial turbulent transport and budgets of the density self-correlation, turbulent mass flux, and turbulent kinetic energy considering a high-Atwood-number spherical implosion case and different broadband and narrowband initial perturbations defined as multimode cosine perturbations that follow a specified power spectrum. El Rafei *et al.* [31,34] presented high-resolution implicit large-eddy simulations (ILESs) of compressible mixing in spherical implosions considering multimode narrowband and broadband initial perturbations consisting of spherical harmonics and multimode cosine perturbations. A high Atwood number ($A_t = 0.9$) corresponding to a density ratio of 20 was examined by the authors, who presented a detailed study of integral growth quantities and bubble and spike heights to provide a detailed understanding of the mixing process and the effect of the initial spectrum of perturbations on the subsequent mixing. The current study complements the findings of those two studies by further analyzing turbulent transport and turbulent budgets to provide a more detailed quantification of the different contributors to the asymmetry in the mixing layer in addition to giving an insight on the contribution of numerical discretization.

The layout of this paper is as follows. Section II details the numerical schemes, the implosion model, and the equations of the initial surface perturbations that are adopted for this study. It also presents the definitions of the various mixing quantities and details the turbulent transport equations of the density self-correlation, turbulent mass flux, and turbulent kinetic energy. In Sec. III different mixing quantities such as the molecular mixing fraction and the normalized mixed mass are presented in addition to the anisotropy tensor. The budgets of all the terms in the transport equations are also discussed. The conclusions of this study are presented in Sec. IV.

II. PROBLEM DESCRIPTION

A. Governing equations and computational methods

The simulations presented here are performed using the high-order fully compressible three-dimensional FLAMENCO spherical solver [72]. A semi-Lagrangian moving mesh algorithm is implemented to ensure mesh motion with the mixing layer. The main aim of the moving mesh

algorithm is to cluster the grid nodes within the mixing layer. The computations solve the compressible multicomponent Euler equations in spherical coordinates. These equations are written in vector form using conservative variables as

$$\frac{\partial \mathbf{U}}{\partial t} + \frac{1}{V}\frac{\partial (A_r \mathbf{F})}{\partial r} + \frac{1}{V}\frac{\partial (A_\phi \mathbf{G})}{\partial \phi} + \frac{1}{V}\frac{\partial (A_\theta \mathbf{H})}{\partial \theta} = \mathbf{S}, \tag{1}$$

where

$$\mathbf{U} = \begin{bmatrix} \rho \\ \rho(u_r - u_G) \\ \rho u_\phi \\ \rho u_\theta \\ \rho E \\ \rho Y_1 \\ \rho Y_2 \end{bmatrix}, \quad \mathbf{F} = \begin{bmatrix} \rho(u_r - u_G) \\ \rho u_r(u_r - u_G) + p \\ \rho(u_r - u_G)u_\phi \\ \rho(u_r - u_G)u_\theta \\ (u_r - u_G)(\rho E + p) + p u_G \\ \rho Y_1(u_r - u_G) \\ \rho Y_2(u_r - u_G) \end{bmatrix}, \quad \mathbf{G} = \begin{bmatrix} \rho u_\phi \\ \rho(u_r - u_G)u_\phi \\ \rho u_\phi^2 + p \\ \rho u_\theta u_\phi \\ u_\phi(\rho E + p) \\ \rho Y_1 u_\phi \\ \rho Y_2 u_\phi \end{bmatrix},$$

$$\mathbf{H} = \begin{bmatrix} \rho u_\theta \\ \rho(u_r - u_G)u_\theta \\ \rho u_\phi u_\theta \\ \rho u_\theta^2 + p \\ u_\theta(\rho E + p) \\ \rho Y_1 u_\theta \\ \rho Y_2 u_\theta \end{bmatrix}, \quad \mathbf{S} = \begin{bmatrix} 0 \\ \frac{2p}{r} + \frac{\rho(u_\phi^2 + u_\theta^2)}{2} \\ -\rho\frac{u_\phi(u_r - u_G)}{r} - \frac{\cos\theta}{\sin\theta}\frac{\rho u_\phi u_\theta}{r} \\ -\rho\frac{(u_r - u_G)u_\theta}{r} + \frac{\cos\theta}{\sin\theta}\frac{\rho u_\phi^2 + p}{r} \\ 0 \\ 0 \\ 0 \end{bmatrix}, \tag{2}$$

where ρ is the mass density; $\mathbf{u} = [u_r, u_\theta, u_\phi]$ represents the velocity vector with u_r, u_θ, and u_ϕ being the velocity components in the radial, polar, and azimuthal directions, respectively; p is the pressure; E is the total energy per unit mass; and Y is the mass fraction. The total energy is defined as

$$\rho E = \rho e + \tfrac{1}{2}\mathbf{u}\cdot\mathbf{u}. \tag{3}$$

The specific internal energy e is defined from the ideal gas equation of state as

$$e = \frac{p}{\rho(\gamma - 1)}, \tag{4}$$

where a constant ratio of specific heats $\gamma = 5/3$ is considered. The vector $\mathbf{S}$ in Eqs. (2) represents the geometric source terms added to the momentum equation to take into account the change in direction of the local vector basis in spherical coordinates. These source terms act as pseudoforces that do not change the magnitude of the momentum. They only change the direction of the momentum vector in the local vector basis. V, A_r, A_ϕ, and A_θ are the exact cell volume and interface areas in the r, ϕ, and θ directions, respectively. The finite volume faces and nodes follow constant radius surfaces for this spherical geometry setup.

For the implosion case considered here, the mesh motion velocity u_G is calculated based on the minimum average radial speed between the spike, bubble, and mixing layer center. The grid velocity decreases linearly outside the limits of the mixing layer, towards the boundaries of the domain. The moving grid approach reduces the numerical dissipation encountered when using Eulerian methods and permits improved resolution of the mixing layer throughout the duration of the implosion, while reducing computational effort since no higher grid resolutions might be needed and maintaining symmetry to machine precision [73]. The mesh velocity is mathematically expressed as

$$u_G(r) = \begin{cases} \min(\overline{u}_s, \overline{u}_b, \overline{u}_{MC}), & R_s \leqslant r \leqslant R_b \\ -\frac{u_G(r=R_b)}{R_{up}-R_b} r + \frac{u_G(r=R_b)}{R_{up}-R_b} R_{up}, & r > R_b \\ \frac{u_G(r=R_s)}{R_s-R_l} r + \frac{u_G(r=R_s)}{R_s-R_l} R_l, & r < R_s, \end{cases} \tag{5}$$

where $\overline{u}_s$, $\overline{u}_b$, and $\overline{u}_{MC}$ represent the average spike, bubble, and mixing layer velocities, respectively. R_s and R_b represent the positions of the spike and bubble, respectively. R_l is the radius at the lower bound of the computational domain and R_{up} represents the radius at the upper bound of the domain. The governing equations are solved numerically using finite-volume Godunov-type high-order methods. The fifth-order MUSCL scheme of Ref. [74] is used for spatial reconstruction and the second-order total variation diminishing (TVD) Runge-Kutta scheme [75,76] is adopted to evolve the solution in time. The low-Mach-number correction method of Ref. [77] is used to reduce the dissipation of the turbulent kinetic energy at the small length scales that are characterized by low Mach numbers. This combination of spatial reconstruction, time integration, and low-Mach-number correction methods has been well established in previous ILESs and more recently in high-resolution Navier-Stokes studies studies of shock-induced turbulent mixing [34,78–83]. Future work will present a more detailed derivation of the governing equations, mesh motion, and numerical methods.

B. Turbulent transport equations and mixing quantities

This study explores the individual transport terms in the turbulent kinetic energy K, density self-correlation b, and turbulent mass flux ρa equations. Those equations were derived by Besnard *et al.* [55] for RANS modeling of mixing in variable-density flows in planar geometries. Advanced variants of the BHR model were presented in Refs. [56,57]. Lombardini *et al.* [67] extended those equations to compressible mixing in spherical geometries and presented different turbulent statistics and mixing measures considering heavy-to-light and light-to-heavy configurations. The current study extends the work of Lombardini *et al.* [67] and presents the turbulent budgets of each of the terms in the turbulent transport equations derived in spherical coordinates for the density self-correlation, the turbulent mass flux, and the turbulent kinetic energy.

The density self-correlation b quantifies how well different fluids are mixed at different stages of the mixing process. This quantity can exhibit non-Boussinesq effects that depend on the density ratio, and the study of those effects can provide understanding of asymmetries in the mixing layer. The density self-correlation is defined as

$$b = -\overline{\rho' v'}, \tag{6}$$

where ρ' is the fluctuating density, $v' = (1/\rho)'$ is the fluctuating specific volume, and the overline represents a surface average. Fluctuations from surface-averaged quantities are given as

$$q'(r, \theta, \phi, t) = q(r, \theta, \phi, t) - \overline{q}(r, t). \tag{7}$$

The turbulent mass flux is a fundamental measure of the rate of energy conversion in variable-density flows [66,84]. This quantity affects the production of turbulent kinetic energy through a direct dependence of the kinetic energy transport equation on the turbulent mass flux. It can also develop asymmetries between the bubble and spike sides, which is helpful in understanding non-Boussinesq effects at high density ratios in spherical implosions. The normalized turbulent mass flux is written as

$$a_i = \frac{\overline{\rho' u_i'}}{\overline{\rho}}, \tag{8}$$

where i represents the direction along which the normalized turbulent mass flux is computed (e.g., r, θ, and ϕ). The turbulent kinetic energy K is defined by taking half of the trace of the Reynolds stress equations:

$$K = \frac{R_{kk}}{2\overline{\rho}}. \tag{9}$$

A Reynolds stress component is defined as

$$R_{ij} = \overline{\rho u_i'' u_j''}, \tag{10}$$

where u'' is the fluctuation from the Favre-like surface average. The Favre-like surface average of any quantity q is written as

$$\tilde{q} = \frac{\overline{\rho q}}{\overline{\rho}}. \tag{11}$$

The fluctuation derived from $\tilde{q}$ is

$$q''(r,\theta,\phi,t) = q(r,\theta,\phi,t) - \tilde{q}(r,t). \tag{12}$$

The transport equation governing the evolution of $b(r,t)$, as derived in Ref. [67], is written as

$$\underbrace{\frac{\partial b}{\partial t}}_{(b\mathcal{U})} + \underbrace{\widetilde{u}_r \frac{\partial b}{\partial r}}_{(b0)} = \underbrace{2a_r \frac{\partial b}{\partial r}}_{b\mathrm{I}} \underbrace{-2\frac{(1+b)}{\overline{\rho}} a_r \frac{\partial \overline{\rho}}{\partial r}}_{b\mathrm{II}} + \underbrace{\frac{\overline{\rho}}{r^2}\frac{\partial}{\partial r}\left(r^2 \frac{\overline{\rho' v' u_r'}}{\overline{\rho}}\right)}_{b\mathrm{III}} + \underbrace{2\overline{\rho}\left(\overline{v'\boldsymbol{\nabla}\cdot\mathbf{u}'} + \frac{1}{r}\overline{v'\cot\theta}\right)}_{b\mathrm{IV}} + ND_b, \tag{13}$$

where bIV is equivalent to

$$2\overline{\rho}\left(\overline{v'\boldsymbol{\nabla}\cdot\mathbf{u}'} + \frac{1}{r}\overline{v'\cot\theta}\right) = 2\overline{\rho}\left(\overline{v\boldsymbol{\nabla}\cdot\mathbf{u}} - \frac{\overline{v}}{r^2}\frac{\partial}{\partial r}(r^2\overline{u_r})\right). \tag{14}$$

The term $b\mathcal{U}$ represents the variation of density self-correlation in time. Terms $b0$ and bI form together the flux of the b term. Term bII is the production of b due to density gradient, bIII is a turbulent transport term, and bIV is the destruction of b due to correlations of specific volume dilatation [67]. ND_b is the numerical discretization effect estimated as the remainder of Eq. (13).

Numerical discretization effects may cause imbalance in the budget through three distinct mechanisms: (i) imperfect statistical convergence, (ii) impact of numerical discretization error, and (iii) difference in the discretization of the budget terms compared to the algorithm implementation in FLAMENCO. For mechanism (i), we believe it is difficult to eliminate for LES where there is a high level of fluctuations in the flow field at high wavenumbers (compared with low-Reynolds-number direct numerical simulation) but as the integral scales are approximately $1/15$ of the domain width this should not be excessive [85]. For item (iii), we have examined the impact of discretization of the budget terms previously [70] and found that for the majority of terms the order of discretization is not critical aside from terms which may show sensitivity to fast acoustic waves. This is not the case here. Thus we are left with mechanism (ii) as the most likely source, hence the terminology "numerical discretization."

The variation of terms bI and bII is affected by the turbulent mass flux production. The transport equation of the radial turbulent mass flux, as derived in Ref. [67], is

$$\begin{aligned}
&\underbrace{\frac{\partial(\overline{\rho}\,a_r)}{\partial t}}_{a_r\mathcal{U}} + \underbrace{\left\{[\boldsymbol{\nabla}\cdot(\overline{\rho}\tilde{\mathbf{u}}\otimes\mathbf{a})]\cdot\mathbf{e_r} - \frac{1}{r}\overline{\rho}\widetilde{u_\theta}a_r\cot\theta\right\}}_{a_r0} \\
&= \underbrace{b\frac{\partial\overline{p}}{\partial r}}_{a_r\mathrm{I}} + \underbrace{\overline{\rho}\left(\overline{v'\frac{\partial p'}{\partial r}}\right)}_{a_r\mathrm{II}} \underbrace{-\overline{\rho}[\mathbf{a}\cdot\boldsymbol{\nabla}(\tilde{\mathbf{u}}-\mathbf{a})]\cdot\mathbf{e_r}}_{a_r\mathrm{III}} + \underbrace{\left(\frac{\overline{\rho' u_r' u_r'} - R_{rr}}{\overline{\rho}}\right)\frac{\partial\overline{\rho}}{\partial r}}_{a_r\mathrm{IV}} \\
&\quad + \underbrace{\overline{\rho}\left\{[\boldsymbol{\nabla}\cdot\overline{\mathbf{a}\otimes\mathbf{a}}]\cdot\mathbf{e_r} - \frac{1}{r}a_\theta a_r\cot\theta\right\}}_{a_r\mathrm{V}} \underbrace{-\left\{[\boldsymbol{\nabla}\cdot\overline{\rho'\mathbf{u}'\otimes\mathbf{u}'}]\cdot\mathbf{e_r} - \frac{1}{r}\overline{\rho' u_\theta' u_r'}\cot\theta\right\}}_{a_r\mathrm{VI}} \\
&\quad \underbrace{-\overline{\rho}\left(\overline{u_r'\boldsymbol{\nabla}\cdot\mathbf{u}'} + \frac{1}{r}\overline{u_r'\cot\theta}\,\overline{u_\theta}\right)}_{a_r\mathrm{VII}} + ND_{a_r},
\end{aligned} \tag{15}$$

where, for any two vectors (c and d, for example),

$$[\nabla \cdot \overline{\mathbf{c} \otimes \mathbf{d}}] \cdot \mathbf{e_r} - \frac{1}{r}\overline{c_\theta d_r}\cot\theta = \frac{1}{r^2}\frac{\partial}{\partial r}(r^2 c_r d_r) - \frac{c_\theta d_\theta + c_\phi d_\phi}{r}. \tag{16}$$

$a_r\mathcal{U}$ is the time rate of change of turbulent mass flux. The terms a_r0 and $a_r\mathrm{V}$ are distribution and transport terms of a_r between the heavy and light fluids. The terms $a_r\mathrm{I}$, $a_r\mathrm{III}$, and $a_r\mathrm{IV}$ are production terms and the term $a_r\mathrm{II}$ is a destruction term. $a_r\mathrm{VI}$ is a turbulent transport of mass flux term and $a_r\mathrm{VII}$ is the destruction of a_r by means of velocity dilatation. The production of turbulent mass flux depends on the density self-correlation through the term $a_r\mathrm{I}$. The term ND_{a_r} is the impact of numerical discretization on Eq. (15).

The turbulent kinetic energy transport equation, as derived in Ref. [67], is written as

$$\begin{aligned}\underbrace{\frac{\partial(\overline{\rho}K)}{\partial t}}_{K\mathcal{U}} + \underbrace{\frac{\partial(\overline{\rho}K\widetilde{u_r})}{\partial r}}_{K0} = &\underbrace{-\left[\mathbf{R} : \nabla\tilde{\mathbf{u}} + \frac{1}{r}\left(R_{\theta\phi}\widetilde{u_\phi} - R_{\phi\phi}\widetilde{u_\theta}\right)\cot\theta\right]}_{K\mathrm{I}} \\ &\underbrace{-\frac{1}{r^2}\frac{\partial}{\partial r}(r^2\overline{p'u_r'})}_{K\mathrm{II}} + \underbrace{\left(a_r\frac{\partial\overline{p}}{\partial r} - \frac{1}{r}\overline{p\cot\theta}a_\theta\right)}_{K\mathrm{III}} \\ &+ \underbrace{\overline{p'\nabla\cdot\mathbf{u}'}}_{K\mathrm{IV}} \underbrace{-\frac{1}{2r^2}\frac{\partial}{\partial r}(r^2\overline{\rho u_i'' u_i'' u_r''})}_{K\mathrm{V}} + ND_K,\end{aligned} \tag{17}$$

where

$$\begin{aligned}\mathbf{R} : \nabla\tilde{\mathbf{u}} + \frac{1}{r}(R_{\theta\phi}\widetilde{u_\phi} - R_{\phi\phi}\widetilde{u_\theta})\cot\theta = &R_{rr}\frac{\partial\widetilde{u_r}}{\partial r} + R_{r\theta}\left(\frac{\partial\widetilde{u_\theta}}{\partial r} - \frac{\widetilde{u_\theta}}{r}\right) \\ &+ R_{\theta\theta}\frac{\widetilde{u_r}}{r} + R_{r\phi}\left(\frac{\partial\widetilde{u_\phi}}{\partial r} - \frac{\widetilde{u_\phi}}{r}\right) + R_{\phi\phi}\frac{\widetilde{u_r}}{r}.\end{aligned} \tag{18}$$

The term $K\mathcal{U}$ is the time rate of change of turbulent kinetic energy and $K0$ is a transport term. $K\mathrm{I}$ represents the exchange of turbulent kinetic energy (TKE) between mean and fluctuating components. The term $K\mathrm{II}$ transports the TKE from the edges of the mixing layer to the interior and $K\mathrm{V}$ transports the turbulent kinetic energy to the edges of the mixing layer [67]. $K\mathrm{III}$ is a production term that depends on the normalized turbulent mass flux a_r, and the pressure dilatation term $K\mathrm{IV}$ is a destruction term. ND_K represents the numerical discretization effect calculated as the residual of the turbulent kinetic energy transport equation. It should be noted that no physical viscous dissipation terms are considered in Eqs. (13), (15), and (17) since only inviscid cases are computed. The terms in the transport equations represent the resolved large-scale components contributing to the variation of density self-correlation, turbulent mass flux, and turbulent kinetic energy, and the effect of the unresolved small scales (unclosed budget terms) is included in the numerical discretization term of each equation.

C. Initial conditions

The aim of this study is to explore the turbulent budgets of different turbulent statistics in spherical implosions. For that purpose, the spherical implosion model from Refs. [86–88] was used. The computational domain consists of a spherical wedge centered at the equator of the sphere shown in Fig. 1. The source region has a high pressure to create a shock wave (Mach approximately 18) that moves into the domain and hits the perturbed interface between the light and heavy fluids, and that is the mechanism that drives the implosion in time. A heavy-light configuration is considered for the implosion model. The molecular weights of the heavy and light fluids are $W_2 = 124.72$ g/mol and $W_1 = 6.24$ g/mol. The radial extent of the domain is $0.05 < r < 1.5$ mm. In the azimuthal and

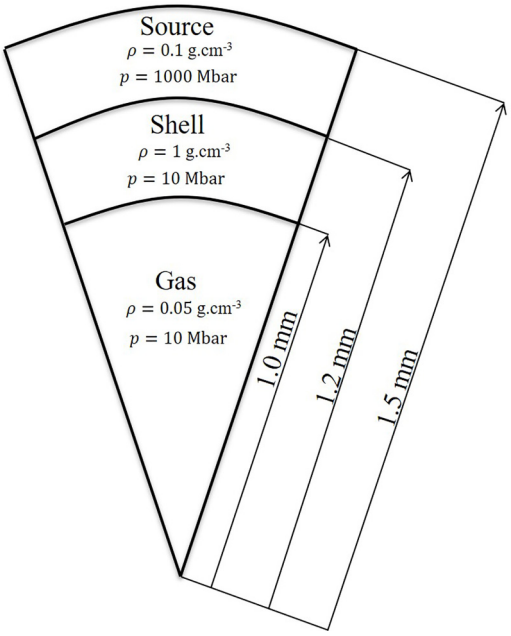

FIG. 1. Initial conditions of the spherical implosion model.

polar directions, $\pi/2 - \pi/8 < \theta, \phi < \pi/2 + \pi/8$, where θ and ϕ represent the polar and azimuthal directions, respectively.

The inner radius of the boundary region depends on time and is defined as

$$r_{\text{src}}(t) = r_{\text{shell}} - v_0 t, \tag{19}$$

where $r_{\text{shell}} = 1.2$ mm and $v_0 = 0.24$ mm/ns. The velocity of the source region depends on time and space via

$$v_{\text{src}}(r, t) = -v_0 r / r_{\text{src}}(t). \tag{20}$$

The reader is referred to Refs. [86–88] for visualizations of the initial profiles of energy, velocity, and density of this implosion model.

In regards to the boundary conditions, an outflow boundary condition is used at the upper boundary to ensure that the reflected waves exit the domain. The lower radial boundary at the core is a reflective condition and the boundary conditions in the polar and azimuthal directions are also reflective. Several computations were repeated using periodic boundary conditions and the postprocessed results are indistinguishable. For the reflective boundary conditions, the flow variables are symmetrized while the normal component of the velocity vector changes signs. A small cutout of radius 0.05 mm is employed at the core of the domain to speed up the calculations and prevent problems of very small time step near the origin due to convergence of the radial grid lines. We selected the size of the cutout in a way to prevent any important changes in the shock timing. We performed several numerical experiments that showed that this choice of cutout size and reflective boundary conditions does not affect the quantities analyzed here in any appreciable manner. Numerical experiments by Flaig *et al.* [86] also showed that this cutout does not have any effects on the growth of small perturbations in the linear phase. The reader is also referred to Ref. [34] for more details about the boundary conditions.

Figure 2 shows a wave diagram from a one-dimensional unperturbed interface implosion setup carried out with 4096 cells in the radial direction. The implosion is driven at $t = 0.5$ ns by the shock wave that hits the interface between the heavy and light fluids. A shock wave is then

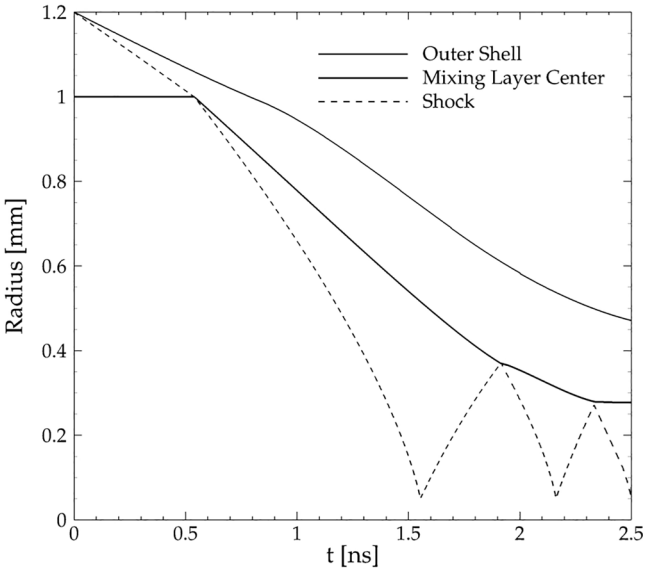

FIG. 2. Wave diagram of the implosion model.

transmitted through the interface and a rarefaction wave is reflected outward since a heavy-to-light fluid configuration is considered [89]. The transmitted shock wave is reflected at the core of the domain near $t \sim 1.5$ ns, which then hits the interface again near $t \sim 1.9$ ns. In this case, both transmitted and reflected waves are shock waves. A second reshock occurs at $t \sim 2.4$ ns before the interface stagnates at $t = 2.5$ ns.

D. Surface perturbation

Different initial spectra of perturbations are considered for the study of the implosion case including NB surface perturbations and BB initial perturbations that are characterized by a wider range of modes compared to narrowband perturbations. The perturbations at the interface between the fluids of different densities are defined in Fourier space as a power spectrum similar to what has been done in Refs. [90] and [78]. The power spectrum of the perturbations has the form

$$P(k) = \begin{cases} Ck^{\alpha}, & k_{\min} < k < k_{\max} \\ 0, & \text{otherwise}, \end{cases} \tag{21}$$

where $\alpha = -2$ for the BB case and $\alpha = 0$ for the NB perturbations. The wave number $k = \sqrt{k_\phi^2 + k_\theta^2}$ is a two-dimensional wave number of the perturbation and C is a constant that has to be chosen to ensure the linearity of the perturbations at the highest wave number. The power spectrum of the broadband and narrowband initial perturbations is shown in Fig. 3.

From the power spectrum equation, the inverse Fourier transform is taken and the amplitude of the perturbations in real space is given using the Euler formula as

$$\begin{aligned} A(\phi, \theta) = \sum_{m,n=0}^{N} [&a_{m,n} \cos(mk_0\phi R_0) \cos(nk_0\theta R_0) + b_{m,n} \cos(mk_0\phi R_0) \sin(nk_0\theta R_0) \\ &+ c_{m,n} \sin(mk_0\phi R_0) \cos(nk_0\theta R_0) + d_{m,n} \sin(mk_0\phi R_0) \sin(nk_0\theta R_0)], \end{aligned} \tag{22}$$

where N is the number of modes and R_0 is the initial interface position. The coefficients $a_{m,n}, b_{m,n}, c_{m,n}, d_{m,n}$ are chosen randomly through the generation of random numbers using a deterministic Mersenne Twister algorithm. This ensures that the standard deviation is proportional

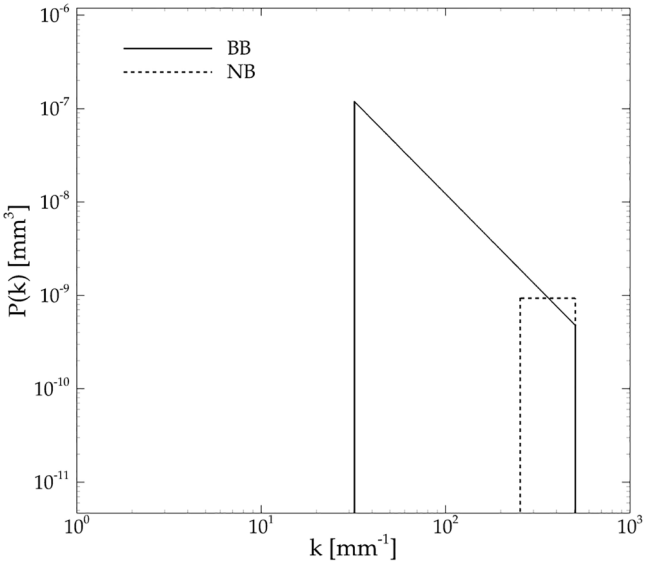

FIG. 3. Power spectrum of the initial broadband perturbations.

to the Fourier coefficients and that the same random numbers are used across multiple grid levels. The mean standard deviation of each mode is given by

$$\sigma_{mn}^2 = \frac{1}{4}\left(\overline{a_{mn}}^2 + \overline{b_{mn}}^2 + \overline{c_{mn}}^2 + \overline{d_{mn}}^2\right) = \frac{1}{2\pi}\frac{P(k_{mn})}{k_{mn}}\Delta k_\phi \Delta k_\theta. \tag{23}$$

The total standard deviation is written as (see Ref. [81])

$$\sigma = \sqrt{C\frac{k^{\alpha+1}}{\alpha+1}(1 - 1/R^{\alpha+1})}, \tag{24}$$

where $R = \frac{k_{\max}}{k_{\min}}$. The mean standard deviation σ_{mn} is written in terms of σ as

$$\sigma_{mn} = \frac{2\pi\sigma}{L}\sqrt{\frac{k_{\max}}{2\pi(R-1)}k_{mn}^{-3}}\sigma_{mn} = \frac{2\pi\sigma}{L}\sqrt{\frac{\alpha+1}{2\pi k_{\max}(1-1/R^{\alpha+1})}k_{mn}^{\alpha-1}}. \tag{25}$$

The constant C in Eq. (21) is determined in the BB case such that the highest wave number is linear ($k_{\max}a_{k\max} = \frac{1}{2}$), which gives

$$C_{BB} = \frac{1}{16k_{\max}}. \tag{26}$$

That is not a great concern in the NB case as it is easy to specify the standard deviation of the perturbation satisfying linear mode amplitude. It should be noted that the perturbations are defined in a way to maintain the mixing layer to be a relatively small proportion of the overall radius, to avoid any perturbations going to the core of the domain at very late times of the mixing process. While the configuration generates significant compressible flow features, the turbulent Mach number defined as $\sqrt{(u_r'^2 + u_\theta'^2 + u_\phi'^2)}/a$ varies significantly from 1.25 at 2 ns down to 0.07 at $t = 2.4$ ns).

A sharp interface is employed here, where the perturbation is employed to assign varying mass fractions to a single layer of mixed cells along the interface at the initial perturbation, a commonly employed approach [91] especially where interfaces in practice are often sharp (solids). For dimensionless times >0.15, Youngs and Thornber [32] show that results from diffuse layer

TABLE I. Broadband and narrowband perturbations setup.

Perturbation type	$\lambda_{\min}$	$\lambda_{\max}$	σ_0	A_t	Mesh size
BB1	$L/64$	$L/4$	$0.1\lambda_{\min}$	0.9	$424 \times 256 \times 256$
BB2	$L/64$	$L/4$	$0.1\lambda_{\min}$	0.9	$848 \times 512 \times 512$
BB3	$L/64$	$L/4$	$0.1\lambda_{\min}$	0.9	$1296 \times 768 \times 768$
NB	$L/64$	$L/32$	$0.1\lambda_{\min}$	0.9	$848 \times 512 \times 512$

computations and sharp layer computations are within just a few percent. The key differences are at very early times, where sharp interfaces have higher initial velocities, and our present computations go well beyond those times.

Table I shows the different specifications of the broadband and narrowband perturbations adopted for this study in terms of standard deviation and minimum and maximum wavelengths. In addition, the grid resolutions chosen for this study are also presented in the table. L in Table I represents the circumference at the initial radial position of the interface ($R_0 = 1$ mm). A high Atwood number ($A_t = 0.9$) is adopted for all the cases and a density ratio $\frac{\rho_2}{\rho_1} = 20$ is considered (ρ_2 and ρ_1 are the densities of the heavy and light fluids, respectively). A summary of the grid convergence of the results can be found in Sec. III A and the Appendix.

III. RESULTS

A. Grid convergence

This section summarizes the grid convergence assessment of the ILESs presented here. The grid convergence study only examines the BB results. The BB layer consists of a wider range of long- to short-wavelength perturbations compared to the NB layer which has a well-defined range of high-wave-number perturbations that is similar to the short-wavelength component of the BB case. The NB layer is expected to be more homogeneous at late times compared to the BB case in which the longer-wavelength perturbations grow slowly without contributing much to the growth at early times. The reader is also referred to Ref. [34], in which the authors presented a grid convergence study of mixedness quantities including the mixed mass, normalized mixed mass, and molecular mixing fraction using the same setup and perturbation types as in the current study, including the NB perturbation. For the NB perturbation, higher power in the high wave numbers initially translates to a more homogeneous NB mixing layer, which prior studies have demonstrated may be sufficiently resolved at a lower mesh resolution than the BB layer [78].

A quantitative measure of the perturbation growth is the integral mix layer width defined as

$$W(t) = \int_0^\infty \overline{f}_1(1 - \overline{f}_1)\mathrm{d}r, \tag{27}$$

where $\overline{f}_1$ is the surface average of the light fluid volume fraction. The integral width gives a good measure of the layer width and can minimize the late-time statistical fluctuations of the mixing width that are observed using threshold measures.

The grid convergence of the integral bubble and spike heights is also investigated. Integral definitions of the heights are used to smoothly approximate the bubble and spike distances in time and that is convenient for modeling purposes where approximations of the bubble and spike velocity and/or acceleration are needed. The integral distances are expressed as weighted averages from the mixing layer center considering a bilinear volume fraction distribution. The bubble and spike heights are then expressed as

$$\overline{h}_b^{(m)} = \left[\frac{(m+1)(m+2)}{2} \frac{\int_0^\infty |r|^m f \mathrm{d}r}{\int_{-\infty}^0 f \mathrm{d}r} \right]^{\frac{1}{m}}, \tag{28}$$

$$\overline{h}_s^{(m)} = \left[\frac{(m+1)(m+2)}{2} \frac{\int_{-\infty}^{0} |r|^m (1-f) \mathrm{d}r}{\int_{-\infty}^{0} (1-f) \mathrm{d}r} \right]^{\frac{1}{m}}, \tag{29}$$

where $m = 1, 2, 3$. Those definitions are adopted from the work of Youngs and Thornber [33] and adapted to the spherical implosion case.

The convergence of the bubble and spike positions is also presented in this section. The spike and bubble positions are reasonably defined from threshold or cutoff measures where the bubble position is the radius at which the surface average volume fraction of the light fluid, $\overline{f}_1 = 0.01$, and the spike position represents the radius at which $\overline{f}_1 = 0.99$. Moreover, this section presents the volume-averaged turbulent kinetic energy in time. The kinetic energy is volume averaged over the width of the mixing layer and is normalized by the impulsive change of velocity imparted by the shock wave at the interface.

Figure 4 plots the integral mixed layer width, bubble and spike positions computed from the threshold measures, integral bubble and spike heights, and volume-averaged turbulent kinetic energy at all the different grid resolutions adopted for this study. The integral bubble and spike heights are calculated using $m = 2$ in this study. The integral mix layer width starts growing after the incident shock wave due to RMI. The small-wavelength perturbations dominate the growth at early times and the long-wavelength perturbations do not contribute much to the growth. The growth is then dominated by the low-wave-number perturbations at late times (after the first reshock). For quite some time, a developing mixing layer will exist, wherein the turbulent kinetic energy is one component within a broadband kinetic energy spectrum caused by the shock interaction. This mixing layer consists of a combination of the kinetic energy associated with linear growth associated with the initial broadband Richtmyer-Meshkov instability (RMI) and that resulting from the low-wave-number end of the fully turbulent part of the mixing layer. Given the perturbation wave numbers typically studied—in the range of modes 6–200, for example—it is not possible to sustain an infrared range of multiple orders of magnitude to the extent as can be seen in planar or homogeneous turbulent cases.

In a computation of a full sphere it could be envisaged that as the turbulent layer continues to evolve, approaching the lowest wave number supportable within the spherical shell, the spherical symmetry of the turbulent layer would be broken by background asymmetries giving rise to a form of three-dimensional decaying turbulence that exhibits an infrared range at modes lower than the fundamental mode on the sphere. With no background asymmetry, it could be expected that a spherical case would become "box constrained" and experience accelerated decay rates similar to box-constrained homogeneous decaying turbulence [92].

In the present computation a sector does not permit this symmetry breaking due to the physical constraint of computing a sector of the sphere. Previous research [85,93] examined constrained RM and homogeneous decaying turbulence (HDT) and demonstrated that turbulence becomes "influenced" by physical constraints (e.g., domain size, sector size) when the integral width is approximately 0.1 times the width of the domain but that the dominant effect is lack of statistical convergence. It is anticipated that the results presented in our paper will hold true when the integral width is smaller than 0.1 times the sector size in ϕ/θ (and as a function of time as it converges). In our case, this is satisfied for the whole calculation. The reader is referred to Ref. [34] for more details on the physics of the integral mix layer width and the difference in behavior between the NB and BB cases. For all those quantities, the greatest difference between the results is observed at the lowest mesh size. Figure 4(a) shows an excellent grid convergence of the mixing layer width at the medium and fine grids where almost no differences can be observed starting from an early stage of the implosion ($t > 1.2$ ns). The greatest difference on the finest grids can be noticed at very early times (just after the passage of the shock wave at the interface) when the layer is being stretched, which is a clear indication of the challenge of accurately resolving the early linear stage of mixing.

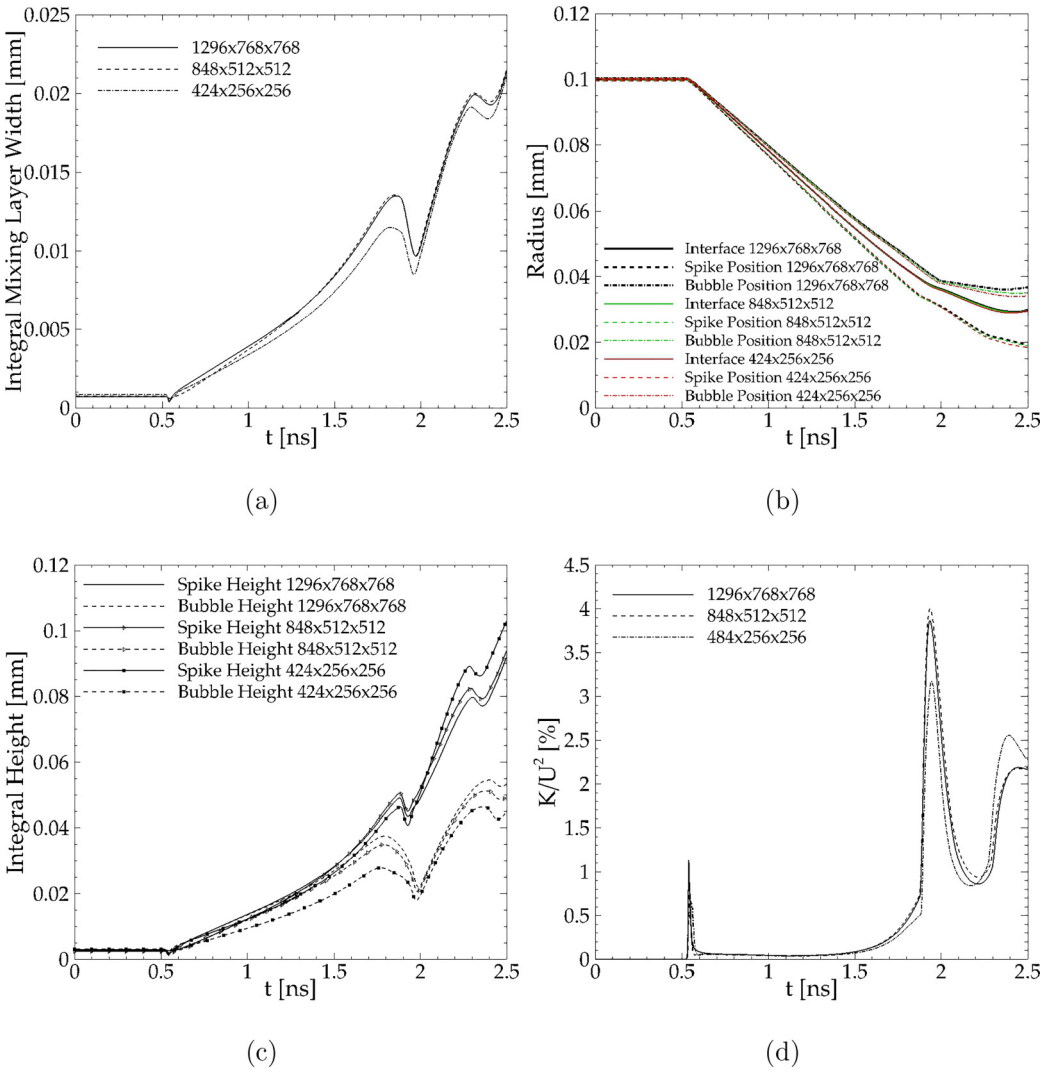

FIG. 4. Grid convergence of (a) integral mixing layer width, (b) spike and bubble positions computed from cutoff measures, (c) integral bubble and spike heights, and (d) normalized turbulent kinetic energy.

A very good grid convergence is observed with the bubble and spike positions shown in Fig. 4(b), although a small difference of ∼2.5% between the medium and fine grids is observed in the time range between the first reshock and stagnation. The maximum difference between the integral bubble and spike heights in Fig. 4(c) at the finest resolutions is ∼6%, which indicates that the convergence of the integral heights is quite reasonable compared to the coarse grid results. Figure 4(d) shows that the volume-averaged turbulent kinetic energy plots at the medium and fine grids are almost identical, which is a good indication of the convergence of the mean quantities.

To the authors knowledge, there is only one published study which examines grid convergence of spatial distribution of budgets for RMI [45] which is both for a planar interaction and employs DNS. DNS studies have considerably lower energy at high wave numbers [39], and thus are relatively easier to converge than LES. The current model implosion considers convergent geometries, multiple reshocks, Rayleigh-Taylor instability, and a very high Atwood number using LES, thus it is expected that convergence would be challenging. With this as context, the Appendix presents

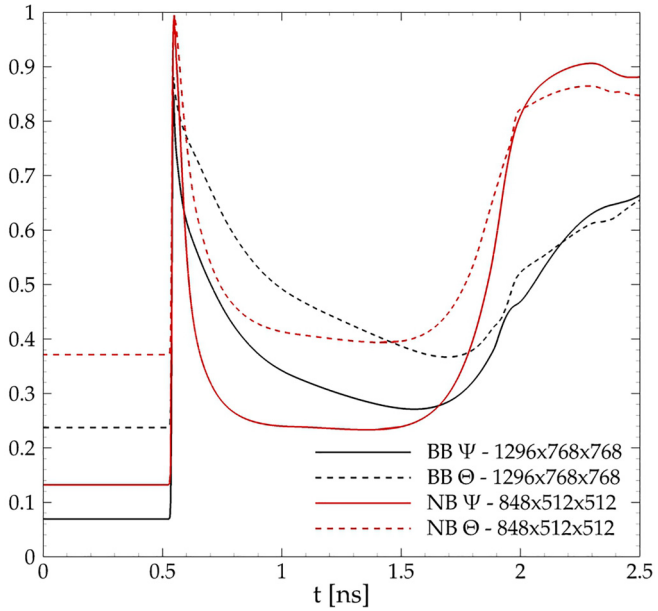

FIG. 5. Variation of normalized mixed mass and molecular mixing fraction in time.

further analysis of the grid convergence of the radial distribution of the turbulent kinetic energy components, the volume fraction distribution, the convergence of the different terms in the density self-correlation, turbulent mass flux and turbulent kinetic energy equations, and the numerical discretization error. Although the chosen measures are not perfectly grid converged (medium indistinguishable from fine), they are sufficiently converged to allow conclusions to be drawn about the dominant flow physics.

Importantly, the numerical discretization (ND) error terms and terms which are impacted by numerical discretization may be seen to be reasonably converged. The former are presented in Fig. 18. One example of the latter is the destruction term [term *b*IV, Eq. (13)] in the density self-correlation equation, which directly measures the impact of numerical discretization in the ILES approach, since the divergence of the velocity field is zero in the absence of diffusive mixing. Examining Figs. 15 and 16, it can be seen that the medium and fine mesh are reasonably converged that the remaining differences may be attributed to statistical convergence over the averaging plane.

To examine statistical convergence, computations were undertaken of the same problem with the same perturbations while changing the initial random number seed. The initial standard deviation and power law remain the same, so changing the random number seed delivers a different instance of the same problem. Results using the different seeds are presented in Fig. 17 for the density self-correlation, turbulent kinetic energy, and turbulent mass flux equations at $t = 2.2$ ns, considering the BB2 case. All the curves have the same general trends but slightly different "noise," which indicates that the results are reasonably statistically converged.

B. Molecular mixing fraction and normalized mixed mass

This section presents two mixedness measures that characterize the amount of mixed fluids within the mixing layer. The first is the normalized mixed mass that gives information on the mixed mass of material within the mixing layer. This quantity is particularly important in ICF applications where it is crucial to understand the mass of ablator that is mixed within the hot spot to reduce that

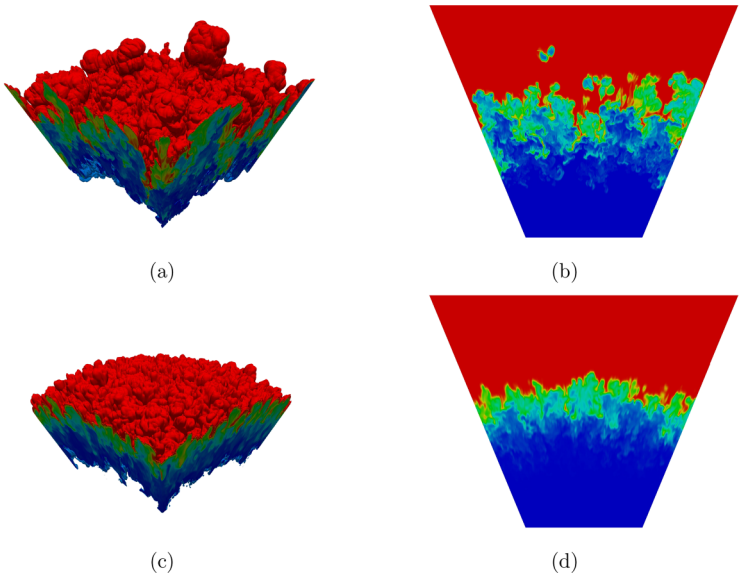

FIG. 6. (a) Isosurfaces of equal volume fraction from the BB3 case, (b) volume fraction contour at $\theta = \frac{\pi}{2}$ from the BB3 results, (c) isosurfaces of equal volume fraction from the NB case, and (d) volume fraction contour at $\theta = \frac{\pi}{2}$ from the NB results. All the contours are taken at $t = 2.5$ ns.

effect. The mixed mass is defined as (see Ref. [94])

$$\mathcal{M} = \int 4\overline{\rho Y_1 Y_2}\mathrm{d}r, \tag{30}$$

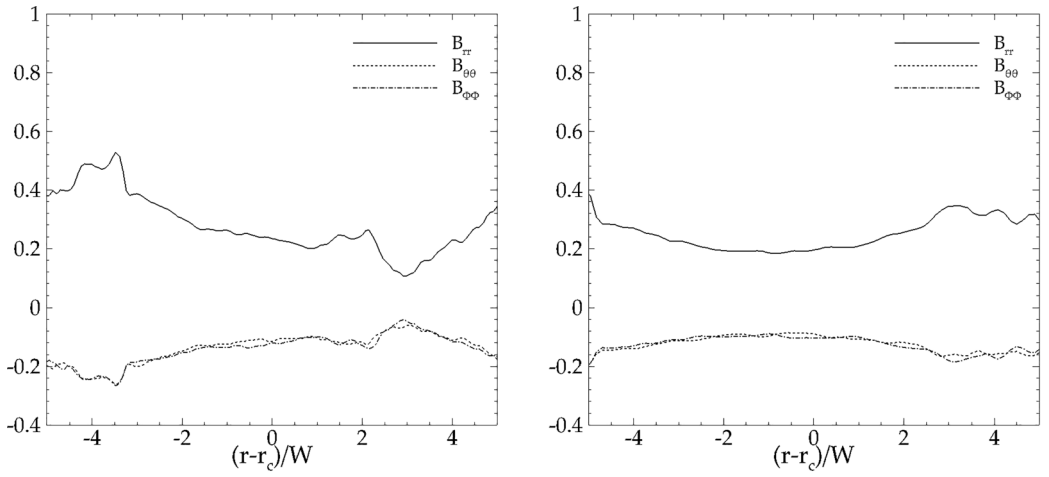

FIG. 7. Radial distribution of the diagonal elements of the anisotropy tensor in (a) BB3 and (b) NB cases at $t = 2.4$ ns.

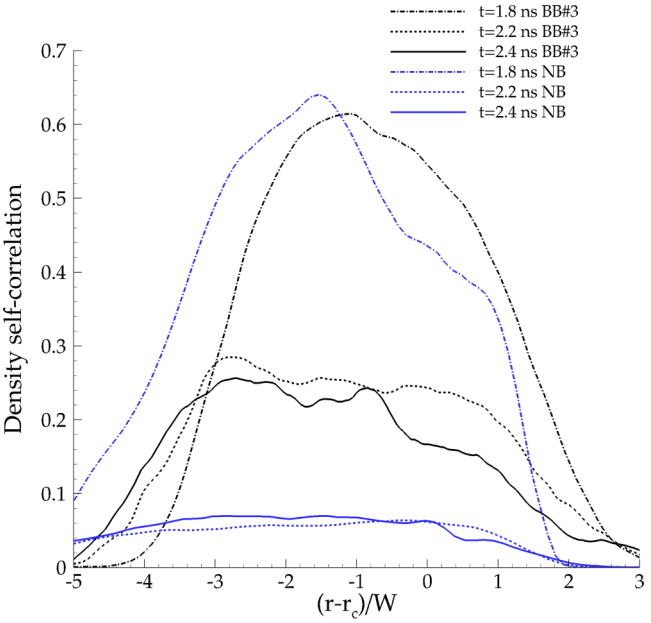

FIG. 8. Radial profiles of the density self-correlation b plotted at different times from the NB and BB3 results.

where Y is the mass fraction of a species. The normalized mixed mass is given as

$$\Psi = \frac{\int \overline{\rho Y_1 Y_2} \mathrm{d}r}{\int \overline{\rho}\, \overline{Y_1}\, \overline{Y_2} \mathrm{d}r}. \tag{31}$$

The molecular mixing fraction is written as

$$\Theta(t) = \frac{\int \overline{f(1-f)} \mathrm{d}r}{\int \overline{f}(1-\overline{f}) \mathrm{d}r}. \tag{32}$$

It represents the ratio of the total chemical product thickness to the maximum thickness due to complete mixing [95]. The study of mixedness parameters provides a further understanding of the mixing activity and the factors contributing to mixing, which can complement the analysis of the different statistics conducted later on in this paper. Figure 5 shows the time variation of the normalized mixed mass and the molecular mixing fraction from the NB and BB3 results. It should be noted here that Θ (or Ψ) $= 1$ represents a fully mixed fluid and a value of zero represents full heterogeneity.

The initial values of Θ and Ψ are due to mixed cells along the initially perturbed interface and that is related to the discrete representation of the interface between the light and heavy fluids. The incident shock wave compresses the perturbations, inducing a substantial reduction in the mixing layer width and a moderate reduction in the thickness of the chemical product, which causes the sharp increase in the mixedness measures at the shock passage. The perturbations then stretch and grow first linearly and then transition to a nonlinear regime due to RTI, RMI, and Bell-Plesset effects causing the decrease in Θ and Ψ. The decay of Ψ is faster before the reshock where elongated structures dominate and where the layer has not yet started transitioning to turbulence and no mixing occurs. The normalized mixed mass Ψ starts increasing again earlier than Θ, inducing an earlier start of transition.

The mixedness measures predict a late-time mixing level of $\sim$0.7 in the BB case, which is consistent with the study in Ref. [69], and $\sim 0.86 \pm 0.02$ in the NB case. This analysis shows that

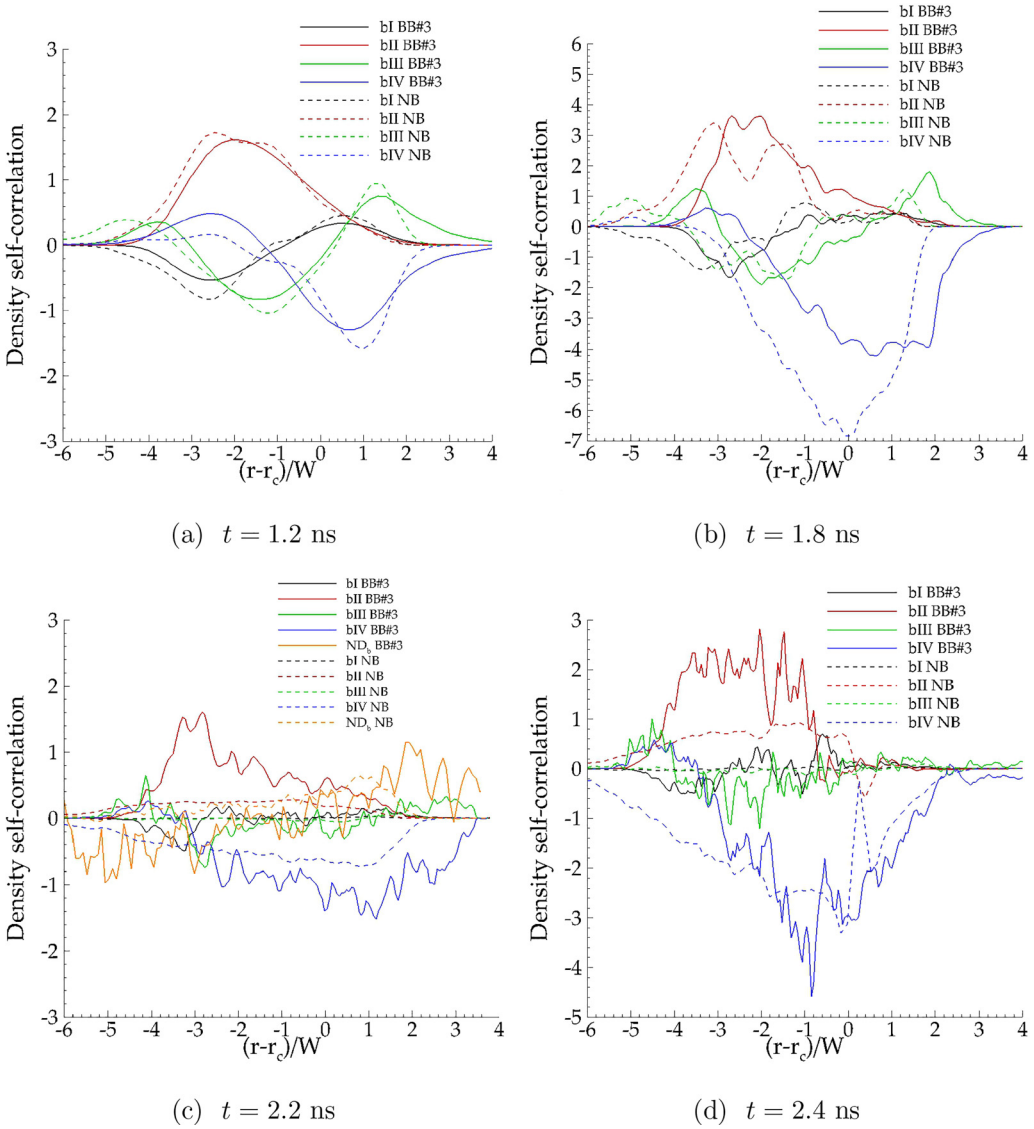

FIG. 9. Budgets of the b transport terms at different times in the NB and BB3 cases.

the BB layer has lower mixing levels compared to the NB case near stagnation. It also shows that the NB layer starts the transition to turbulence earlier than the BB case and that was observed from the earlier increase in the mixedness quantities before the reshock in the NB case. This means that the narrowband layer is more homogeneous at late times compared to the BB case. The same conclusion has also been shown in Ref. [34], where the authors compared the mixedness quantities from the NB and BB cases at the same grid resolution ($848 \times 512 \times 512$) and showed that the NB layer transitions faster to turbulence. The lower mixing in the BB case is due to the long-wavelength perturbations that are still contributing to the growth of the layer after the reshock. Those long-wavelength perturbations do not contribute much to the mixing, which means that unmixed fluid still exists and turbulent structures would grow on top of the long-wavelength perturbations. A recent study [81] investigated compressible mixing in NB and BB planar cases and

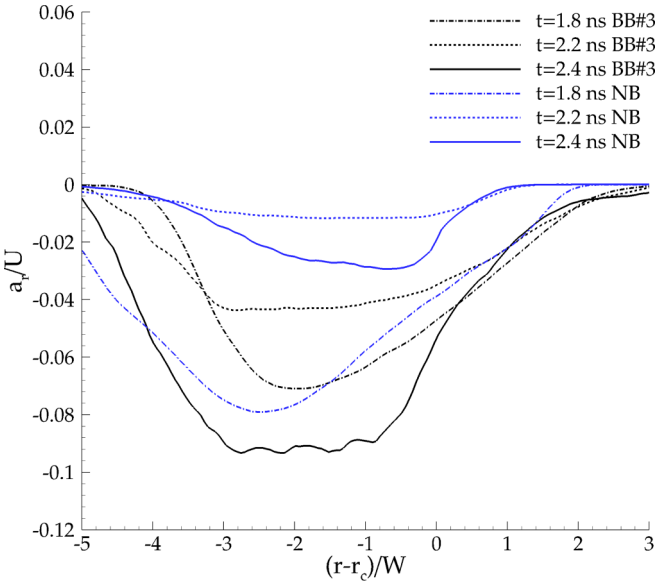

FIG. 10. Radial profiles of the normalized turbulent mass flux a_r plotted at different times from the NB and BB3 results.

showed that the value of the molecular mixing fraction increases as the exponent m in the power spectrum definition increases towards zero, which is consistent with the higher values of Θ in the NB spherical case presented here. Moreover, Thornber *et al.* [78] showed that a reshock increases the value m for modes whose amplitude is mostly due to RM of the previous shock; thus, the multiple reshocks considered in the current implosion model act to push the power spectrum of the perturbations in the BB case to values that are higher than -2. These factors explain the higher value of Θ in the BB case compared to single-shock BB planar cases recently investigated in Ref. [81], where Θ had a value of $\sim$0.39 in the low-Atwood-number BB planar case.

Figure 6 shows visualizations of the mixing layer state from both the NB and BB3 results before stagnation at $t = 2.5$ ns, using isosurfaces of equal volume fraction distribution and 2D volume fraction slices at $\theta = \frac{\pi}{2}$. A wide range of length scales is observed in the BB case where the layer consists of multiscale structures and large bubbles and spikes growing in addition to the smaller turbulent length scales. The NB case is more isotropic and more homogeneous relative to the BB case. In both cases, the transition to turbulence is well under way.

C. Anisotropy

This section examines anisotropy in the given three-dimensional spherical implosion case considering narrowband and broadband initial perturbations. The mechanism of perturbation growth is complicated since it is driven by RMI, RTI, and Bell-Plesset effects. The contributions of all those factors and also the choice of initial conditions affect the anisotropy in the mixing layer. The large-scale anisotropy is measured here by the Reynolds stress anisotropy tensor, given as

$$B_{ij} = \frac{R_{ij}}{R_{kk}} - \frac{1}{3}\delta_{ij}. \tag{33}$$

The diagonal elements of the anisotropy tensor are bounded between $-1/3$ and $2/3$, where $B_{ii} = \frac{2}{3}$ corresponds to 100% of the turbulent kinetic energy in the i direction and $B_{ii} = -\frac{1}{3}$ corresponds to no energy in that direction. A value $B_{ii} = 0$ corresponds to isotropic turbulence. Figure 7 shows the cross-stream profiles of the diagonal components of the anisotropy tensor near stagnation in both the

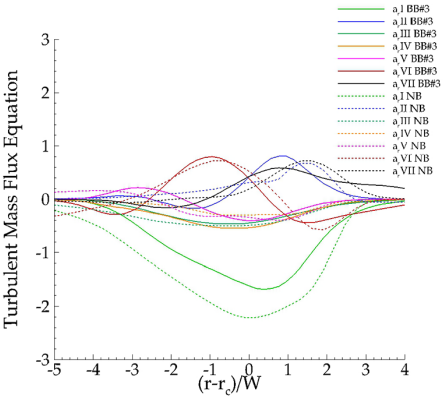

(a) $t = 1.2$ ns

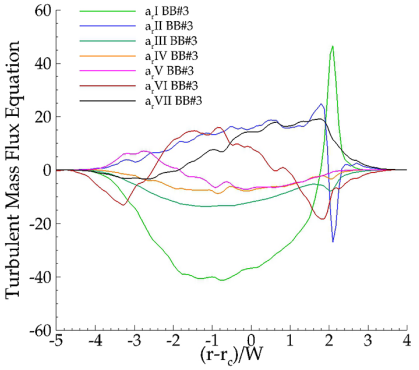

(b) $t = 1.8$ ns - BB

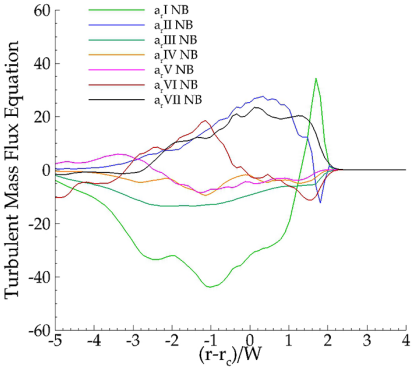

(c) $t = 1.8$ ns - NB

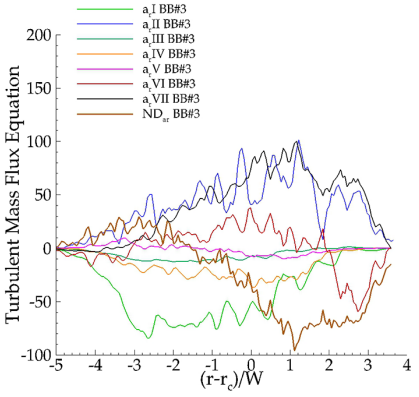

(d) $t = 2.2$ ns - BB

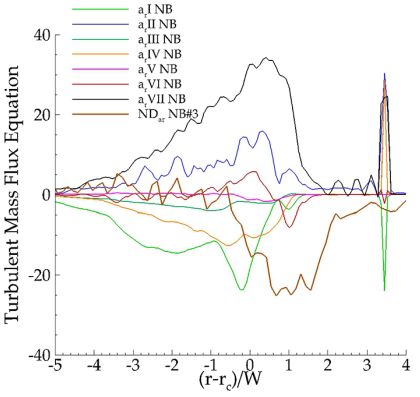

(e) $t = 2.2$ ns - NB

FIG. 11. Individual terms in the a_r transport equation at different times. [(h) and (i)] The variation of the volume-averaged terms in time in the BB3 and NB cases.

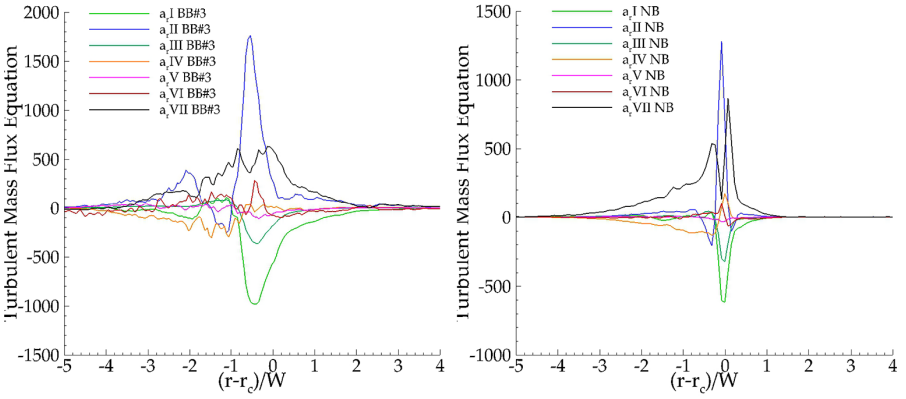

(f) $t = 2.4$ ns - BB (g) $t = 2.4$ ns - NB

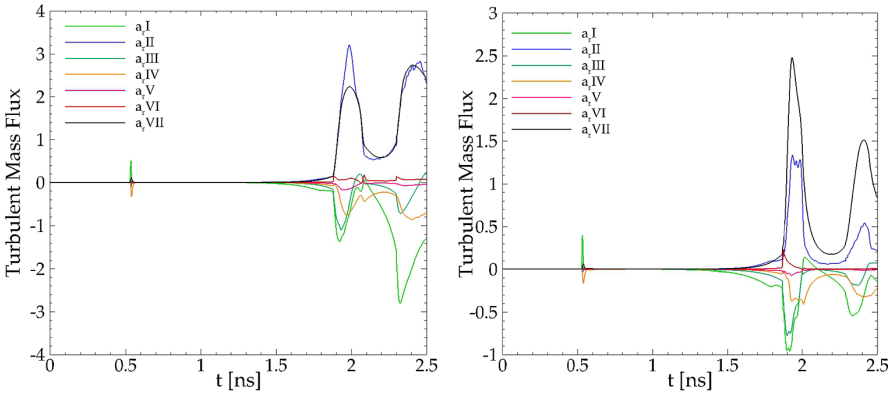

(h) Volume averaged terms, BB#3 (i) Volume averaged terms, NB

FIG. 11. (*Continued.*)

NB and BB cases. This figure demonstrates that the normal stresses at the end of the implosion are showing strong anisotropy. The normal component B_{rr} has an average value of ∼0.3 which accounts for 65% of the kinetic energy in the broadband case and an average value of ∼0.24 in the narrowband case which represents approximately 57% of the kinetic energy. This behavior is consistent with previous RMI and RTI studies in both planar and spherical geometries (see Refs. [66,67,69,96]). The radial component of the anisotropy tensor in both the NB and BB cases dominates compared to the polar and azimuthal components that represent 17.5% each in BB case and 21.5% each in the NB case.

The BB case shows an asymmetry in the distribution of B_{rr} with a larger anisotropy on the spike side compared to the narrowband case which is more homogeneous. That is related to the persistent growth of the long-wavelength perturbations in the BB case at late times that contribute to this asymmetry compared to the NB case where the perturbations are at later dimensionless time and more isotropic.

D. Density self-correlation transport

The density self-correlation b is a fundamental quantity in second-moment RANS modeling of variable density mixing and was the subject of several previous numerical and experimental

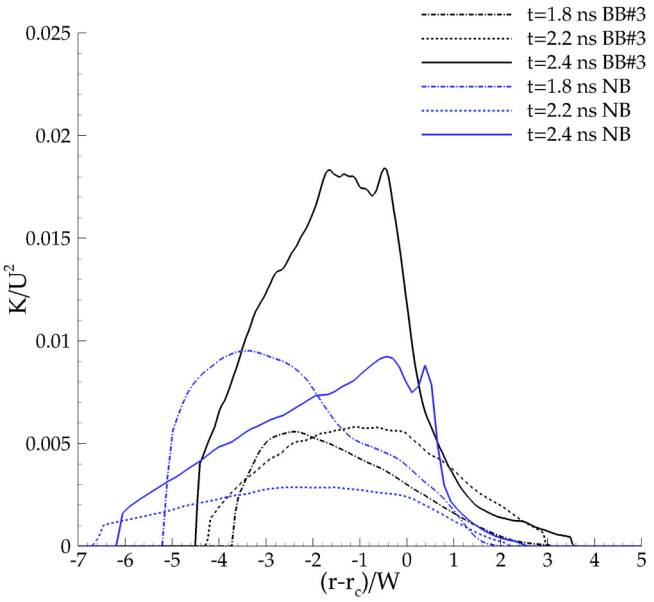

FIG. 12. Radial profiles of the turbulent kinetic energy K plotted at different times.

RMI and RTI investigations (see Refs. [45,60–67]). The density self-correlation is a measure of how well fluids are mixed, where a value $b = 0$ represents a perfect mixture. It provides insights into turbulent transport and non-Boussinesq effects across the mixing layer and also affects the production of turbulent mass flux through the dependence of the a_r equation on b as explained in Sec. II A. Non-Boussinesq effects include asymmetries in the mixing layer around the mixing center, as opposed to a Boussinesq behavior where the density difference is small and the layer is symmetrical [66,67].

Figure 8 shows the radial surface-averaged distribution of b within the mixing layer in the narrowband and broadband cases at different times where transition to turbulence and mixing are most relevant. The comparison between NB and BB cases provides more insights into the effect of the initial spectrum of perturbations on turbulence statistics at late times. In all cases, the peak density self-correlation decreases in time within the mixing layer, indicating an increase in mixing between the light and heavy fluids. The density self-correlation distribution within the mixing layer at $t = 1.8$ ns is characterized by a single peak behavior that is located close to the mixing center but shifted towards the spike side. As the layer grows in time and transition to turbulence increases, the density self-correlation spreads in an asymmetric fashion where the curves are shifted towards the spike side and higher values are observed near the spikes, indicating more mixing on the bubble side where the bubbles interact near the mixing center. That is a clear indication of highly non-Boussinesq effects at this high density gradient considered across the layer.

The peak value of b in both BB3 and NB cases at $t = 1.8$ ns is between 0.6 and 0.65, indicating partial mixing near the first reshock. The NB curve at $t = 1.8$ ns is shifted towards the spike relative to the layer center, indicating higher asymmetry between the bubble and spike sides. That observation is also confirmed in the study of integral quantities presented from the NB results in Ref. [34], which showed more asymmetry in the NB case compared to the BB layer throughout the mixing process. The peak value of b decreases and reaches $b \sim 0.26$ in the BB3 case near stagnation where the highest mixing levels are observed and that is consistent with the peak values presented in Refs. [67,69]. The distributions are in good qualitative agreement with the planar RMI results of Ref. [45].

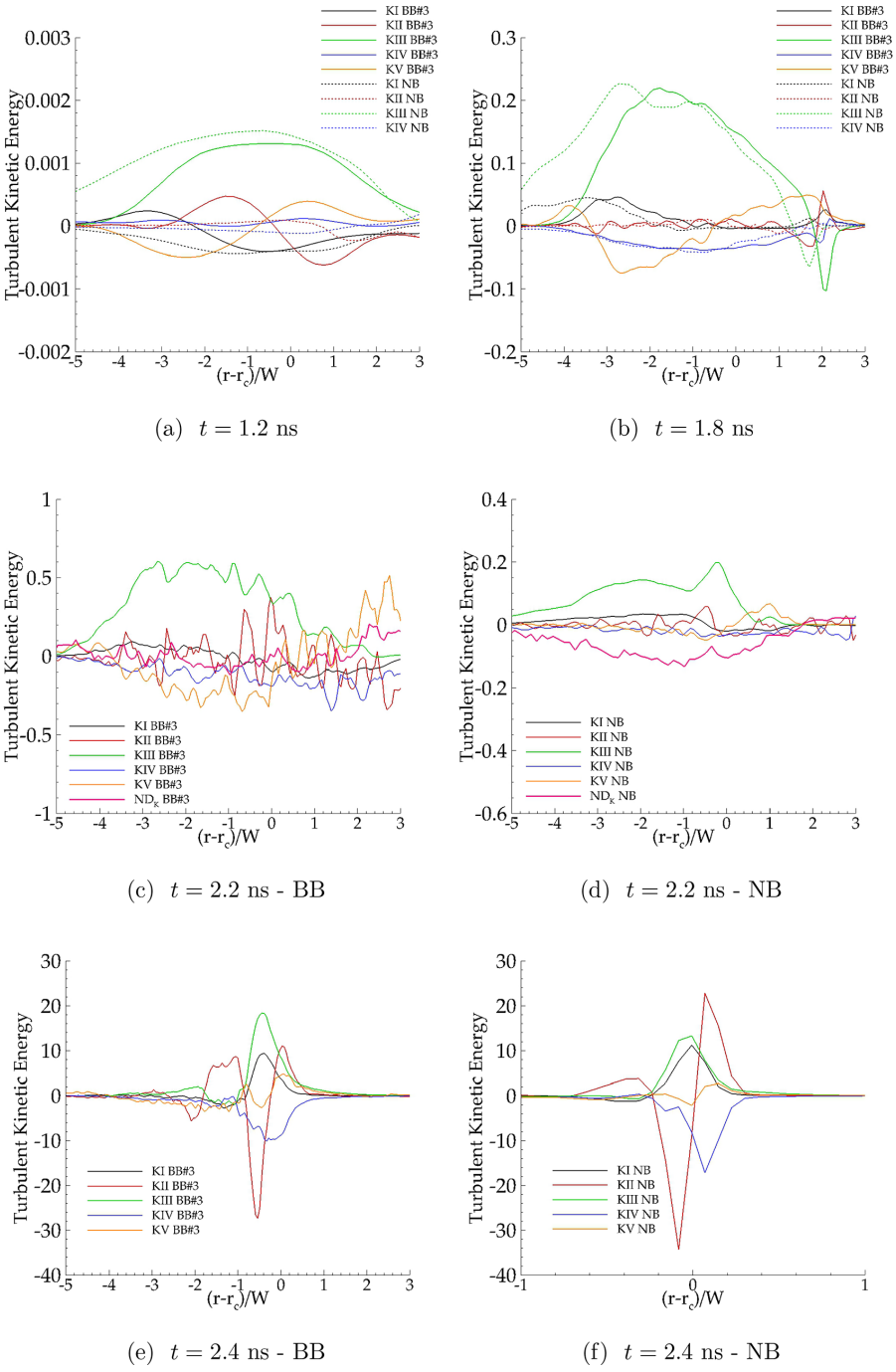

(a) $t = 1.2$ ns

(b) $t = 1.8$ ns

(c) $t = 2.2$ ns - BB

(d) $t = 2.2$ ns - NB

(e) $t = 2.4$ ns - BB

(f) $t = 2.4$ ns - NB

FIG. 13. Individual terms in the K transport equation at different times.

The peak value of b in the NB case at $t = 2.4$ ns is $\sim$0.07, which is approximately four times smaller than the BB case, due to the persistent long-wavelength perturbation growth dominating the BB layer at late times and not contributing much to mixing. The NB case has mainly

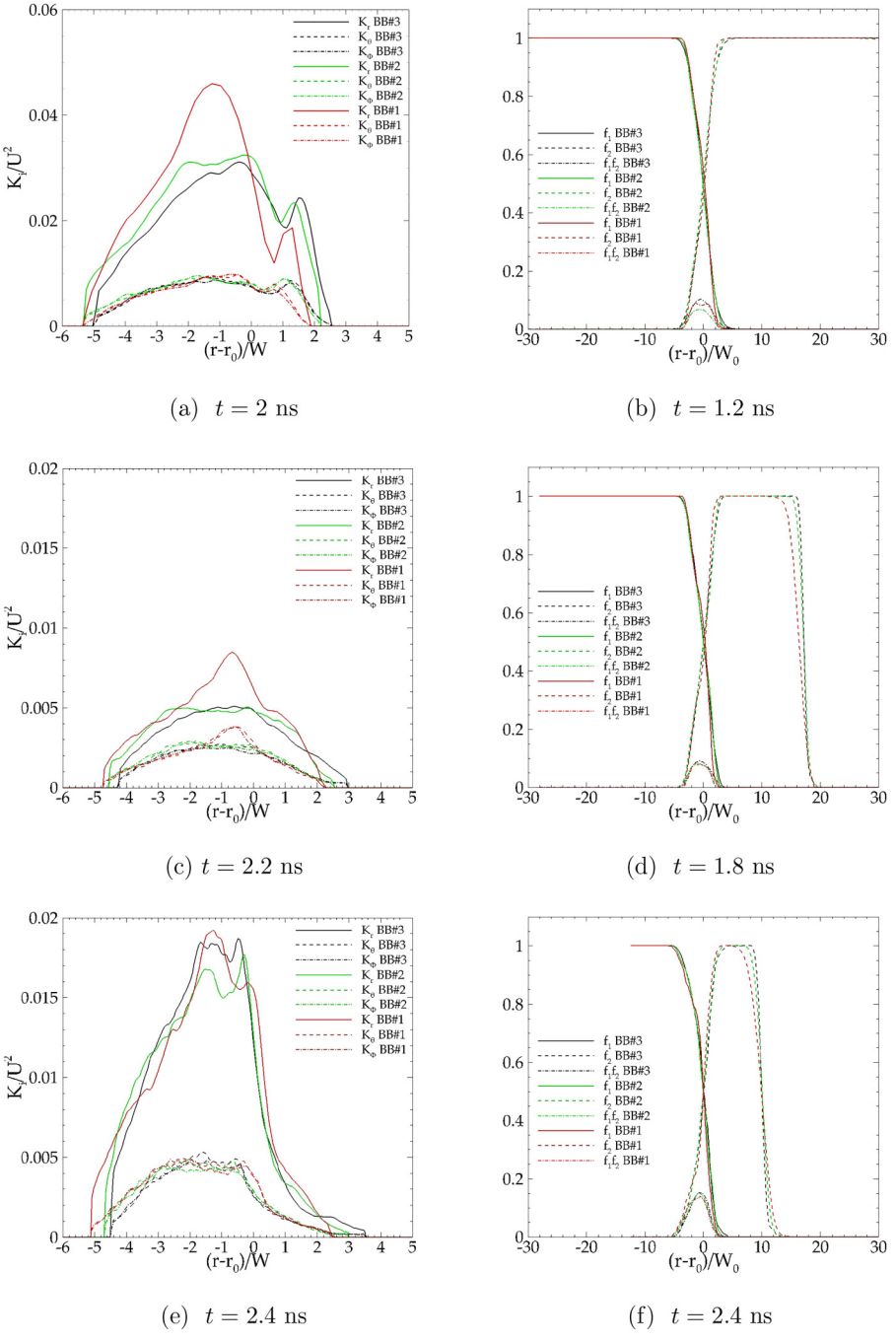

(a) $t = 2$ ns (b) $t = 1.2$ ns

(c) $t = 2.2$ ns (d) $t = 1.8$ ns

(e) $t = 2.4$ ns (f) $t = 2.4$ ns

FIG. 14. Grid convergence study of turbulent kinetic energy components (K_r, K_θ, K_ϕ) and volume fraction distributions at different selected times.

high-wave-number perturbations that have transitioned to a more isotropic turbulent layer and hence inducing more mixing at the final stages of the computation, making the NB layer more homogeneous. It should be noted that the density self-correlation does not change much between

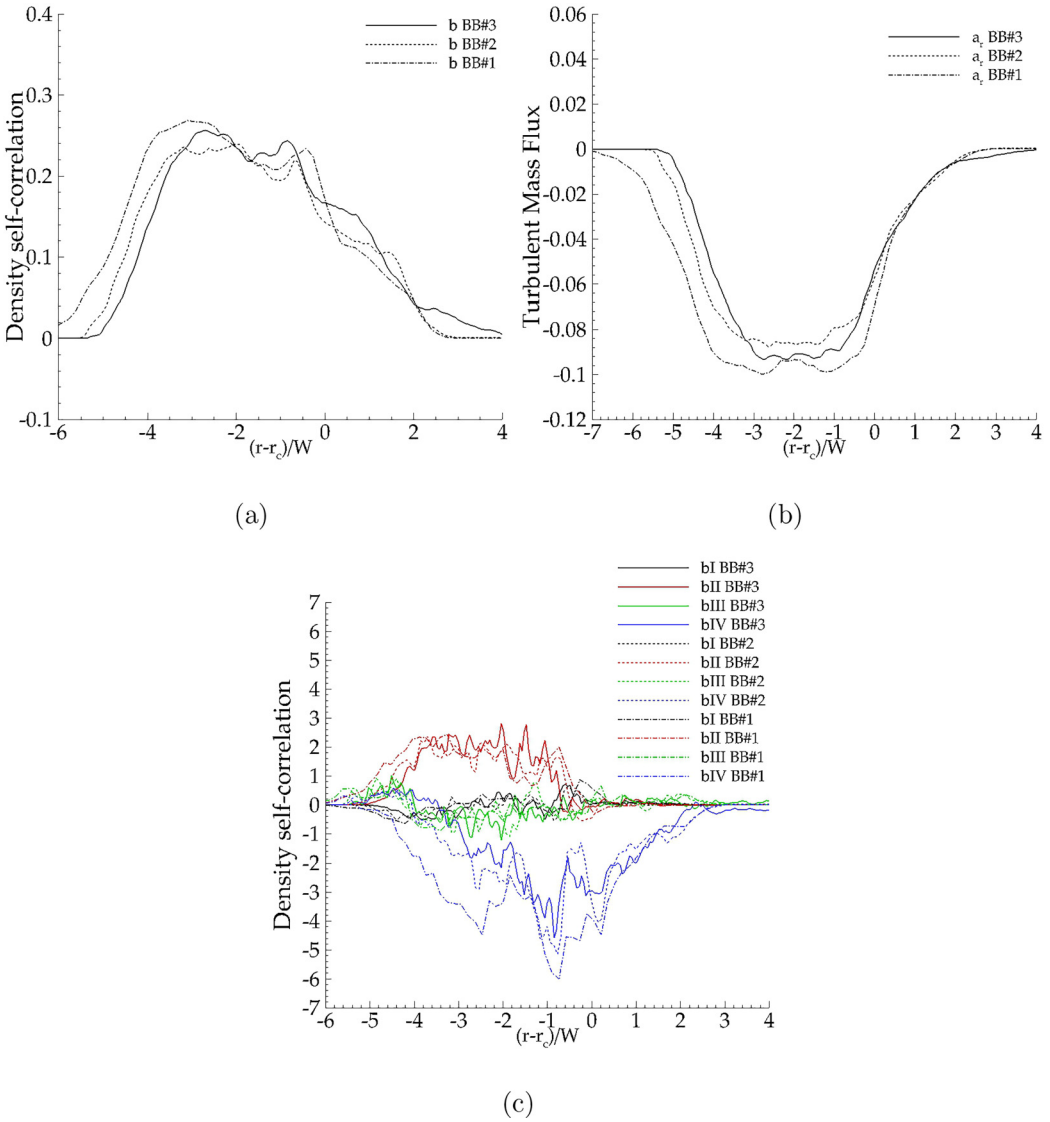

FIG. 15. Grid convergence study of (a) density self-correlation b, (b) normalized turbulent mass flux A_r at $t = 2.4$ ns, and (c) b terms.

2.2 and 2.4 ns and the biggest difference is observed between 1.8 and 2.2 ns. That is due to the first reshock that is exciting the smaller scales, pushing forward the transition and mixing within the layer.

Figure 9 presents the individual terms on the right-hand side of the density self-correlation transport equation [Eq. (13)] in both NB and BB3 cases. The term bI contributes to the distribution of the density self-correlation in the mixing layer; it is characterized by a bimodal trend that transports b from the light to the heavy side. The second term is bII; it represents the production of b by the density gradient and is characterized by a single peak behavior that is shifted in the direction of the spike throughout the late stages of the mixing process.

The asymmetry in the production terms of b also explains the asymmetry in the b curves shown in Fig. 8. The term bIII is the one containing the triple correlation; it is responsible for the transport of

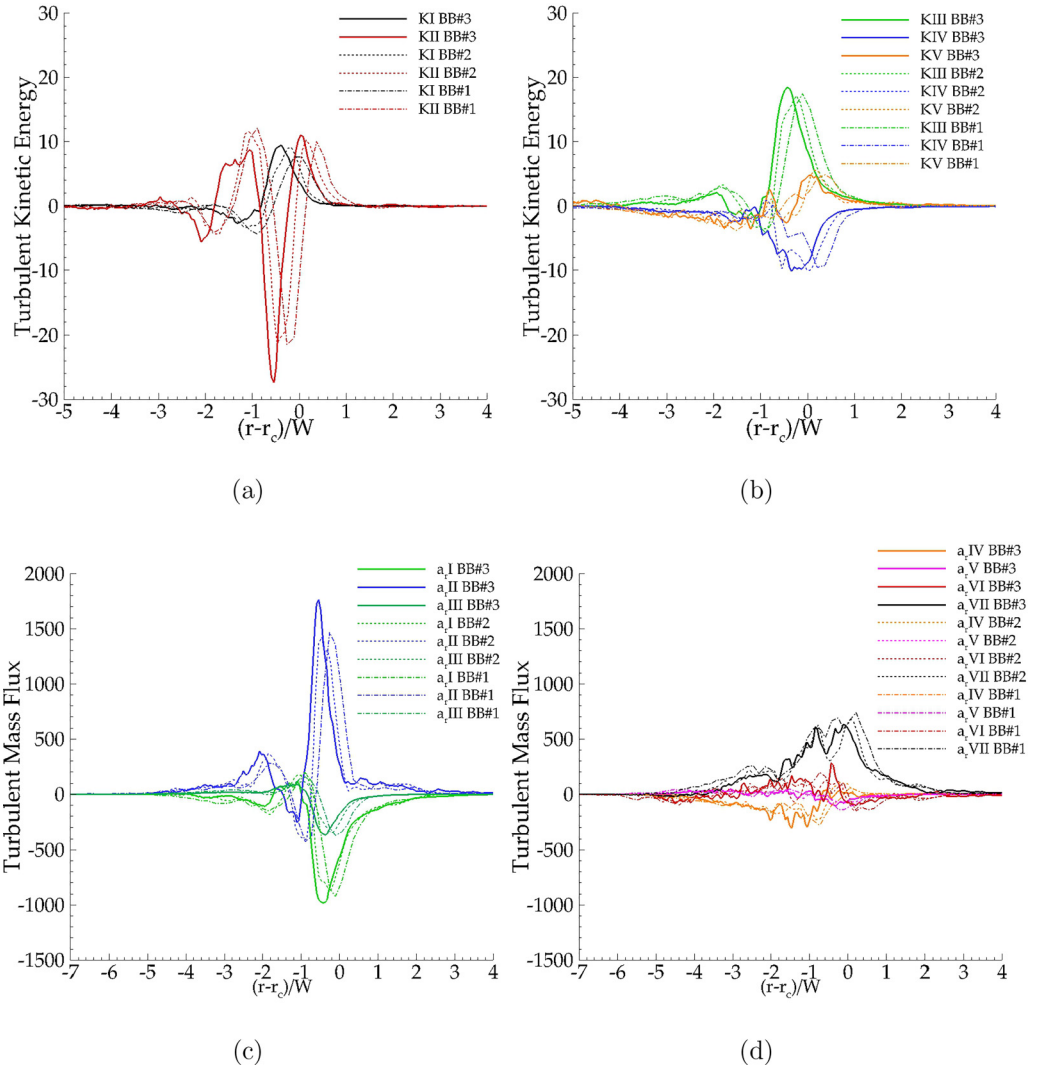

FIG. 16. Grid convergence study of [(a) and (b)] K terms and [(c) and (d)] A_r terms at $t = 2.4$ ns.

b towards the edge of the mixing layer and the spreading of the density self-correlation profiles. This term is closed using gradient diffusion hypothesis [55,56] that yields a modeled form that includes the effect of diffusion of density self-correlation in the equation. The trends of bI, bII, and bIII are similar in behavior to that observed in the study by Livescu *et al.* [66] for RTI planar cases and the RMI experiments of Tomkins *et al.* [62]. The last term, bIV, is responsible for the decay of b by means of specific volume dilatation; it shows a radial distribution characterized by a small positive peak near the inner edge of the mixing layer (where the spike is located) and a large negative peak on the bubble side. This term is closed using decay models where the dissipation of b is modeled using a turbulent viscosity that is a function of the turbulent kinetic energy and turbulent length scale [55,56]. The negative region of bIV dominates the distribution at late times compared to the small positive peak, inducing a small contribution to the density self-correlation production by bIV near the spike position and more decay near the mixing center and bubble side in the BB case. In the

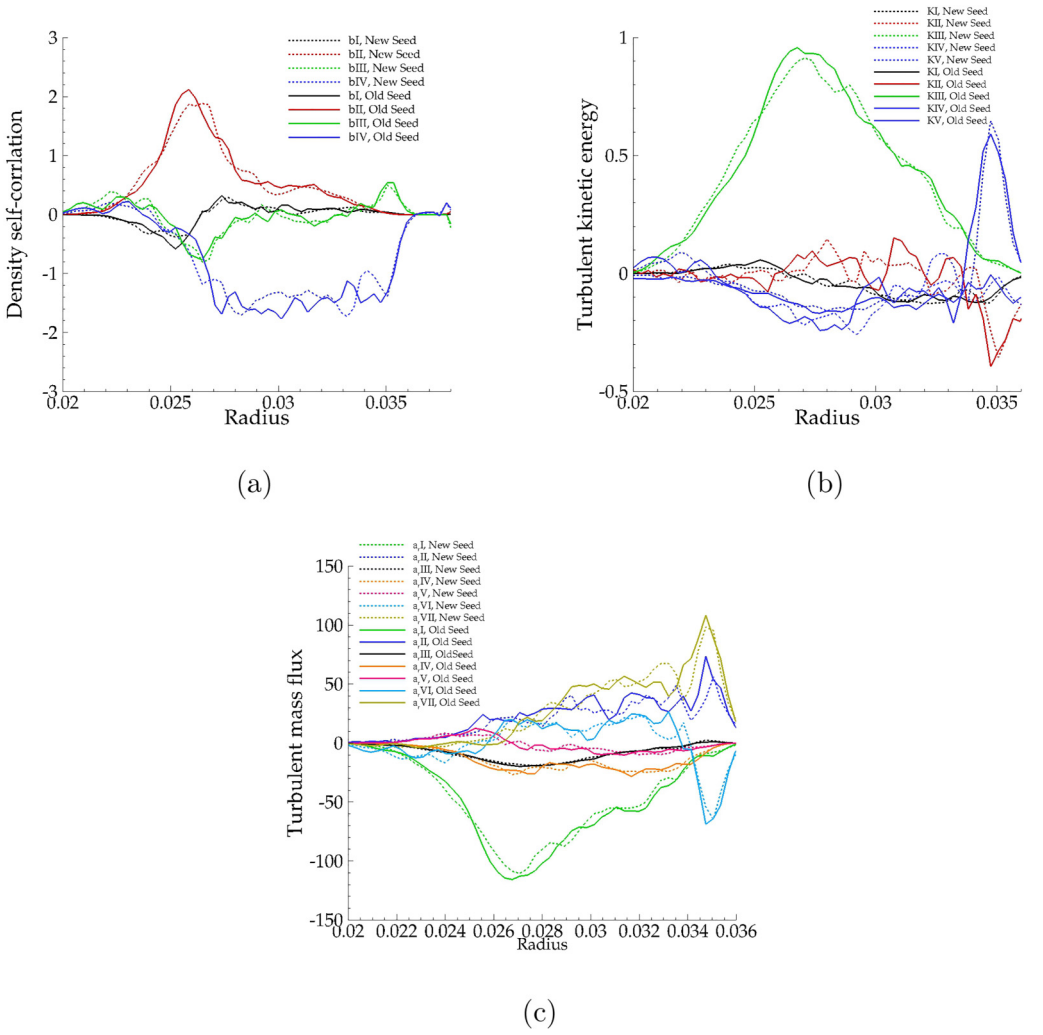

FIG. 17. Statistical convergence analysis, examining results using different initial perturbation seeds for the density self-correlation, turbulent kinetic energy, and turbulent mass flux equations at $t = 2.2$ ns using the BB2 case.

NB case, the term bIV purely represents a destruction with negative values throughout the mixing layer at late times.

It is important to note that the term bIV directly quantifies the implicitly modeled diffusion of density self-correlation by the numerical method. For example, if numerical diffusion may be represented by Fickian diffusion, we would have the following result:

$$\boldsymbol{\nabla} \cdot \mathbf{u} = -\boldsymbol{\nabla} \cdot \left(\frac{D}{\rho} \nabla \rho \right), \tag{34}$$

where D in these ILESs represents solely numerical diffusion. While the actual truncation error of the algorithm is considerably more complex, we expect a similar impact.

The numerical discretization term calculated at $t = 2.2$ ns shows that the effect of ND_b is grid converged and not negligible in both the NB and BB cases. It acts to reduce the change of b by reducing the gap between the production and destruction terms and has positive values near the

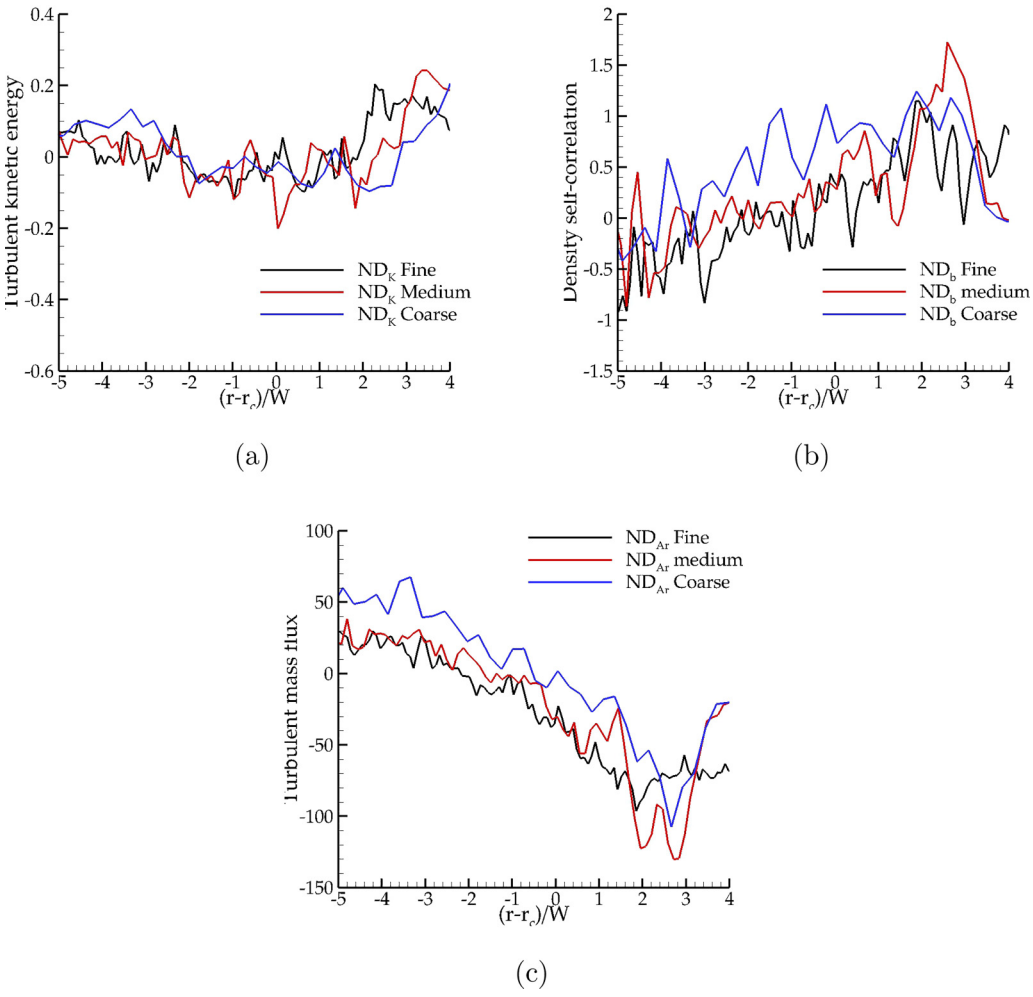

FIG. 18. Grid convergence study of (a) ND_K, (b) ND_b, and (c) N_{a_r} at $t = 2.2$ ns from the BB case.

bubble side and negative values at the spike side. The impact of under-resolution on the evolution of the density self-correlation is expected to be felt through each of the production, advection, diffusion, and destruction terms, and all these effects are incorporated in the numerical discretization term in this ILES. The reader is referred to Ref. [59] for more details on the modeling of unresolved density self-correlation and the different terms affecting the gradient of b at the unresolved scales. The impact of the smaller scales represented by the numerical discretization is most significant on the diffusion and dissipation of b terms that are closed using turbulent models. This means that the contribution of the numerical discretization is not solely expected to be dissipative and also acts in a diffusive manner and can have positive contribution to the rate of change of b, as shown in Fig. 9(c).

The budgets of the density self-correlation terms in the NB case are quite similar to the BB3 case at the early stages of mixing that are dominated by linear or nonlinear growth. Near the first reshock, the destruction in the NB case is higher than the BB layer and shows more non-Boussinesq effects and more asymmetry of all the terms towards the spike side. After the first reshock, where most of the turbulent activity and mixing occur, the terms bII and bIV are the dominant terms in the b-transport equation; thus, these terms are key in understanding the differences in the density self-correlation distribution observed in Fig. 8.

At late times of the mixing process ($t = 2.2$ and 2.4 ns), the production term bII from the NB results has an average maximum value that is approximately four times smaller than the BB case, which contributes to the higher values of b in Fig. 8 at late times. Although bIV is on average similar between the two cases, the destruction in the narrowband case is much larger than the BB case relative to the density self-correlation state within the layer at $t = 2.2$ and 2.4 ns. In other words, the destruction terms have similar magnitude in both the NB and BB cases at late times; however, b is four times smaller in the NB case, which means that the destruction has a much larger effect in the NB case. The terms bI and bIII are negligible in the NB case and small compared to bII and bIV in the BB case.

E. Turbulent mass flux transport

This section provides an analysis of the turbulent mass flux transport and budgets. The rate of conversion of potential energy to kinetic energy is directly proportional to the turbulent mass flux as shown in Ref. [66]; thus, the analysis of this quantity gives more understanding of the effect of mass flux on the turbulent kinetic energy production and of the asymmetry in turbulent transport within the mixing layer.

Figure 10 plots the distribution of the surface average radial normalized turbulent mass flux a_r defined in Eq. (8) at different times during the implosion process. The radial normalized turbulent mass flux is shown within the limits of the mixing layer where most of the turbulence activity is located and a_r is normalized by the initial impulsive change of velocity U that is due to the passage of the incident shock wave. The radial position is taken with respect to the mixing layer center r_c and normalized by the integral mix layer width W. The study of mixedness quantities in Sec. III B showed that the transition to turbulence and mixing starts near the first reshock, which is why the distribution of a_r is only plotted at $t = 1.8$, 2.2, and 2.4 ns, where the turbulent mass flux is more prominent compared to the early stages of the implosion where no turbulence occurs.

In the BB3 case, the normalized mass flux a_r decreases after the reshock due to compression and then starts increasing again to peak near stagnation. In contrast, the normalized turbulent mass flux in the NB case did not have a noticeable recovery after the reshock. Moreover, the peak normalized turbulent mass flux in the BB case near stagnation is approximately three times (in absolute value) higher than the NB case at $t = 2.4$ ns, which means that the rate of conversion of potential energy to kinetic energy in the NB case at late times is less than what is observed in the BB case. The low-wave-number perturbations in the BB case that keep growing after the reshock and contribute to the growth of the layer boost the conversion of potential energy to kinetic energy. However, the NB mixing layer at this late stage is more homogeneous and more mixing between the length scales and less growth of the layer width occur. These results are similar to previous incompressible RTI studies that used ILESs in Cartesian geometries, considering similar initial conditions with the current study (see Refs. [97–99]).

In all cases, the peak normalized turbulent mass flux is located within the mixing layer and is shifted towards the spike side, meaning that most of the mass flux is associated with the spikes that are more energetic and that penetrate further into the domain compared to the bubbles that are closer to the mixing center as shown in Fig. 4(b). The distribution of a_r shown here is a clear indication of the highly non-Boussinesq asymmetries.

Figure 11 shows the budgets of the terms on the right-hand side of the turbulent mass flux transport equation [refer to Eq. (15)] from the NB and BB3 results. The terms a_rI, a_rIII, and a_rIV represent the production of turbulent mass flux. The term a_rI is the largest at early times until the first reshock, which indicates that, in cases where no mixing occurs or large amounts of nonmixed fluids exist, this term will affect the most the rate of change of the mass flux. It should also be noted that the term a_rI depends on the density self-correlation and the closure of this term requires using the transport equation of b shown previously.

The destruction term a_rII, which includes the specific volume-pressure gradient correlation, is one of the dominant terms at the late stages of the implosion and shows the highest levels of turbulent

mass flux destruction near the bubble side, which contributes to the asymmetry observed in Fig. 10. This term is modeled as a decay that is related to the turbulent kinetic energy, the turbulent length scale, and the turbulent mass flux as suggested in Refs. [55,56,59]. By looking at Figs. 11(a)–11(e), the term a_rII is of similar magnitude and sign to the destruction term a_rVII in the BB case, which is not the case in the NB results. At $t = 2.4$ ns, a_rII shows the highest peak near the mixing center in all cases and has an averaged value similar to a_rVII in the BB results. Those observations are also confirmed in Figs. 11(h) and 11(i), which show the variation of the volume-averaged terms in the a_r equation within the mixing layer in time. The term a_rIV is symmetric at the mixing center at early times ($t = 1.2$ ns) but then becomes asymmetric at late times and shifted towards the spike side.

The asymmetry in the a_r-terms distribution at the different stages of the mixing process is again a manifestation of the high density gradient across the layer that induces high non-Boussinesq effects. The unbalanced production and destruction terms also explain the continuous variation of the normalized turbulent mass flux shown in Fig. 10.

The budgets of the NB case at early times are similar to the BB case but show higher values of production, a_rI. That could be explained by the higher density self-correlation on the spike side at this stage due to the faster growth of the short-wavelength perturbations to nonlinear regimes compared to the BB layer. At late stages of the mixing process ($t = 2.2$ and 2.4 ns), the budgets of the turbulent mass flux terms in the NB case are lower than in the BB case, indicating lower energy conversion rate due to the NB layer being at a later dimensionless time with more mixing and more homogeneity. Figures 11(h) and 11(i) show that the budgets of terms a_rV and a_rVI are negligible in the NB case and their effect can be just canceled from the transport equation. Those figures show that a_rV and a_rVI have overall close magnitudes (which is not the case at the reshocks) but with opposite sign in the BB case; thus, they cancel each other at the late times in the BB case. It should be noted that the triple correlation term a_rVI can be modeled using a gradient diffusion hypothesis (see Refs. [55,56,59]) and this modeling represents the diffusion effect in the turbulent mass flux transport equation.

The numerical discretization term ND_{a_r} calculated at $t = 2.2$ ns has a dominant effect near the bubble side and the peak value is of similar magnitude to the physical term a_rI. The diffusion and destruction terms that are closed using the gradient diffusion hypothesis and decay models are the most sensitive to the effect of the small scales and thus include a diffusion effect, which explains the small positive contribution of ND_{a_r} near the spike side.

F. Turbulent kinetic energy transport

Figure 12 shows the radial distribution within the mixing layer of the turbulent kinetic energy K from the NB and BB3 results. The kinetic energy K is normalized by the square of the initial impulsive velocity change U^2 induced by the incident shock wave. In both NB and BB cases, the turbulent kinetic energy distribution before the reshock is shifted towards the spike side, which is a representation of the more energetic spikes before the reshock. The NB case shows a higher peak of kinetic energy before the reshock, which is expected due to the faster transition of the perturbations to turbulence at this stage in the NB case compared to the BB layer.

The first reshock causes the compression of the perturbations and deposits vorticity within the layer while accelerating the transition to turbulence. The highest levels of turbulent kinetic energy are observed near stagnation and the peak of K is located close to the mixing center. The kinetic energy given from the BB results is approximately two times higher than the NB case. Near stagnation, the NB layer is not growing much and the density gradient effect is also lower due to more mixing, making the layer more homogeneous compared to the BB case that has dominant growth from the long-wavelength perturbations and more density gradient effects at this stage inducing growth and increasing kinetic energy.

Figure 13 shows the budgets of the individual terms in the K equation at different times in the NB and BB3 cases. The turbulent kinetic energy distribution in the NB case shows more asymmetry towards the spike side before the reshock due to the faster transition of the short-wavelength

perturbations to turbulence. At late times, the budgets of turbulent transport terms in the NB case are lower than the BB3 terms, which is, as explained before, due to the more homogeneous nature of the NB layer at this stage. In all cases, the production term KIII shows the largest peak in the inner region of the layer throughout the mixing process, which is an indication of the importance of the turbulent mass flux on the energy conversion since this term depends on a_r. The highest levels of turbulent kinetic energy production are shifted toward the spike side, which explains the asymmetry in the kinetic energy distribution in Fig. 12.

The term KII is a transport term that redistributes the kinetic energy from the edges to the interior of the mixing layer. The transport term KV represents the triple correlation in Eq. (17); it is not negligible as shown in Fig. 13 and contributes to the transport of energy to the edges of the layer. This term has negative values in the region of highest kinetic energy production (term KIII) and positive values toward the bubble side. The gradient diffusion hypothesis proposed in Ref. [55] could be used to provide a closure for the diffusion effect of this term.

The pressure dilatation term KIV has a negative distribution across the mixing layer and is one of the main contributors to the destruction of kinetic energy. The closure of this term can use eddy viscosity approaches to represent the decay of kinetic energy. The mean velocity gradient term KI is small compared to the other terms before the first reshock and then becomes non-negligible at the late stages of the mixing process due to the reshocks that induce an increase in the velocity gradient. This term decays between the first and second reshocks due to the decay of the velocity gradient after the first reshock and then it is expected to increase again at the second pulse before stagnation.

Figures 13(e) and 13(f) show that the peak of KI near the mixing center has approximately the same magnitude as the peak of KIV but with opposite sign, which means that those two peaks cancel each other, inducing maximum kinetic energy production at this stage through the term KIII. The production of kinetic energy dominates the resolved destruction at late times, which explains the increase of the turbulent kinetic energy at the late stages in Fig. 12. The effect of the small scales is shown through the numerical discretization term ND_K that is calculated at $t = 2.2$ ns. While not negligible, it is small relative to the resolved terms and the magnitude is insensitive to grid resolution. In the NB case, ND_K is uniformly dissipative due to the later dimensionless time which is achieved by the mixing layer and the smaller turbulent length scales.

IV. CONCLUSIONS

Turbulence statistics and quantitative budgets of density self-correlation, turbulent mass flux, and turbulent kinetic energy have been examined from the results of high-resolution three-dimensional high-Atwood-number spherical implosion simulations. The simulations were performed using a semi-Lagrangian high-order spherical algorithm implemented in the FLAMENCO solver considering different broadband and narrowband initial multimode perturbations. This study reported on several quantities of interest to give a more in-depth understanding of the mixing activity, transition to turbulence, and asymmetries in the mixing process and also to quantify the importance of the budgets of the terms on the right-hand side of the transport equations while considering different perturbation spectra. The effect of numerical discretization was computed as the residual of the turbulent transport balance was also investigated.

The analysis of the mixedness quantities, including the molecular mixing fraction and the normalized mixed mass, showed that the NB layer reaches a later dimensionless time where the scales are more mixed, making the layer more homogeneous compared to the BB layer that has a persistent growth from the long-wavelength perturbations that are not contributing much to the mixing. The study of the normal components of the anisotropy tensor showed strong anisotropy in both the NB and BB cases with the NB case being more isotropic and homogeneous compared to the BB layer, which showed more asymmetry and anisotropy on the spike side. The radial component of the turbulence kinetic energy accounts for most of the kinetic energy (65% in the BB case and 57% in the NB case) as opposed to the azimuthal and polar components, which represent a smaller fraction of the energy (17.5% each in BB case and 21.5% each in the NB case).

The mean density self-correlation was investigated and showed highly non-Boussinesq effects and also indicated higher mixing in the NB case, consistent with the observations from the mixedness parameters. The budgets of the terms in the b equation showed that the production and destruction terms are dominating the late stages of the mixing process and the other transport terms are negligible. The effect of the destruction terms on the density self-correlation is much larger in the NB case relative to the state of density self-correlation within the layer, which contributes to the higher density self-correlation values in the BB case. In all cases, the highest change in the density self-correlation was observed between 1.8 and 2.2 ns due to the first reshock that increases quickly the layer mixing.

The examination of the mean radial normalized turbulent mass flux and mean turbulent kinetic energy showed high asymmetry in the distribution of a_r and turbulent kinetic energy across the mixing layer, which is also a manifestation of the initial high-density gradient effect considered in this study. This is due to the fact that the spikes are more energetic compared to the bubbles that are interacting near the mixing center. This study showed higher levels of turbulent mass flux and turbulent kinetic energy in the BB case, or in other words, higher potential to kinetic energy conversion rates. This is related to the low-wave-number perturbations in the BB case that dominate the growth at late times making the spike and bubbles spread further into the domain, enhancing the conversion of potential energy to kinetic energy at the late stages of the mixing process.

The budgets of the terms on the right-hand side of the turbulent mass flux equation showed that production due to density self-correlation and pressure gradient, the destruction due to the specific volume-pressure gradient correlation, and the destruction by velocity dilatation are the dominant terms across the layer in both the NB and BB cases. The re-distribution and transport terms a_rV and a_rVI are negligible in the NB case and cancel each other in the BB case since they have close magnitudes but with opposite signs. The turbulence budgets from the turbulent kinetic energy transport equation indicated the importance of the turbulent mass flux on energy conversion since the production term that depends on a_r showed the largest peaks across the mixing process. This study also showed that the triple correlation term is not negligible and requires accurate modeling to close the problem. The triple correlation term moderates the production of kinetic energy in the regions where the production terms are maximum and contributes to the production of TKE near the bubble side. The effect of the transport term KII is negligible and could be canceled out from the budget equation. The production terms dominate the destruction at the late stages of the mixing process, inducing higher turbulent kinetic energy at this stage. Moreover, production due to pressure dilatation and mean velocity gradient terms and transport due to pressure velocity fluctuations are not negligible after the reshock, which increases the complexity of modeling this equation.

The study of the residuals of the turbulent transport equations showed that the numerical discretization modeling the effect of the small scales contributes to both diffusion and dissipation and may have positive or negative sign in the computed budgets. It is also shown to be quite insensitive to grid resolution in the grid sizes employed here. That was clear in the density self-correlation and turbulent mass flux equations where the numerical discretization had positive impact on the rate of change of b and a_r in some of the regions within the mixing layer. The numerical discretization moderated the change of b by reducing the gap between the production and dissipation terms in the density self-correlation equation and showed a largely dissipative effect in the a_r and K equation. Finally it was noted that destruction of b through the term bIV is principally due to numerical diffusion, and this provides an interesting quantification of numerical discretization, shown here to be reasonably grid converged.

ACKNOWLEDGMENTS

The authors would like to acknowledge the computational resources at the National Computational Infrastructure provided through the National Computational Merit Allocation Scheme, as well

as the Sydney Informatics Hub and the University of Sydney's high performance computing cluster Artemis, which were employed for all cases presented here. They would like to also acknowledge discussions with Prof. D. Youngs. The authors would also like to thank the anonymous reviewers for their helpful comments to improve the paper.

APPENDIX

Figures 14–16 show the grid convergence assessment of the radial components of the turbulent kinetic energy distribution, the volume fraction distribution, and the grid convergence of the budgets in the density self-correlation, turbulent mass flux, and turbulent kinetic energy distribution. It also shows a statistical convergence analysis where computations of the same problem are undertaken with the same perturbations (BB2 case) while changing the initial random number seed. Results using the different seeds are presented in Fig. 17 for the density self-correlation, turbulent kinetic energy, and turbulent mass flux equations at $t = 2.2$ ns. The grid convergence analysis of the residual terms is presented in Fig. 18.

The radial distribution of the turbulent kinetic energy components in the radial, azimuthal, and polar directions and the volume average distribution plots in Fig. 14 show a reasonable convergence where the average error varies between 8% and ∼11% at the highest resolutions. Figures 15 and 16 present the radial distribution of the density self-correlation and turbulent mass flux and the budgets of all the terms on the right-hand side of the turbulence transport equations considering different grid resolutions at $t = 2.4$ ns.

The two simulations with the highest resolutions in Figs. 15(a) and 15(b) show that the density self-correlation and turbulent mass flux have converged on average across the mixing layer. The budget terms show that the statistics are oscillatory and more challenging to converge. However, the results at the highest grid resolutions are on average matching compared to the coarse grid results.

Table II shows the L_2 error norms, defined as

$$L_2 = \frac{\sqrt{\frac{1}{N}\sum_N (f_i - f_{\text{fine}})^2}}{f_{\text{peak}}}, \tag{A1}$$

where f_i are the individual terms (e.g., bI, bII, etc.) for $i =$ (coarse, medium) with N points and f_{peak} is the peak value of that term at that time instant. The results are shown in Table II. For the terms bI–bIII, the coarse and fine mesh results have a normalized L_2 norm less than 2% of the peak value from the fine mesh result. The term bIV has a normalized L2 norm of 18% of the peak value for the coarse mesh, and 8.2% for the medium mesh when compared with the fine mesh. It is converging at an order of 1.15, as may be expected for a complex flow with shock waves and material discontinuities. Thus although it is not as well converged as the other terms, it is showing a clear trend towards convergence. This analysis also provides an indicator that statistical errors may be the most likely remaining dominant error in these surface-averaged quantities for bI–bIII.

The greatest difference between the medium and fine grids is observed near the spike side, which is the most challenging small vortical large-scale structure to resolve. This impact of the spikes on the kinetic energy budgets was also observed in previous planar RMI studies [70,79]. Based on the

TABLE II. Normalized L_2 error norms for the b equation.

Quantity	L_2 coarse	L_2 medium	Order of convergence
bI	0.018	0.013	0.47
bII	0.013	0.010	0.41
bIII	0.016	0.019	−0.18
bIV	0.185	0.083	1.15

analysis presented here, the results of the highest grid resolution BB case (BB3) have a good grid convergence and are adopted for the subsequent discussions.

[1] L. Rayleigh, Investigation of the character of the equilibrium of an incompressible heavy fluid of variable density, Proc. London Math. Soc. **S1-14**, 170 (1883).

[2] S. G. Taylor, The instability of liquid surfaces when accelerated in a direction perpendicular to their plane, Proc. R. Soc. London A **201**, 192 (1950).

[3] D. H. Sharp, Overview of Rayleigh-Taylor instability, Physica D **12**, 3 (1984).

[4] J. Nuckolls, L. Wood, A. Thiessen, and G. Zimmermann, Laser compression of matter to super-high densities: Thermonuclear (CTR) applications, Nature (London) **239**, 139 (1972).

[5] J. D. Lindl, P. Amendt, R. L. Berger, S. G. Glendinning, S. H. Glenzer, S. W. Haan, R. L. Kauffman, O. L. Landen, and L. J. Suter, The physics basis for ignition using indirect-drive targets on the National Ignition Facility, Phys. Plasmas **11**, 339 (2004).

[6] J. D. Lindl, O. Landen, J. Edwards, E. Moses, and N. Team, Review of the National Ignition Campaign 2009-2012, Phys. Plasmas **21**, 020501 (2014).

[7] O. A. Hurricane, D. A. Callahan, D. T. Casey, P. M. Celliers, C. Cerjan, E. L. Dewald, T. R. Dittrich, T. Döppner, D. E. Hinkel, L. F. B. Hopkins, J. L. Kline, S. L. Pape, T. Ma, A. G. Macphee, J. L. Milovich, A. Pak, H. S. Park, P. K. Patel, B. A. Remington, J. D. Salmonson *et al.*, Fuel gain exceeding unity in an inertially confined fusion implosion, Nature (London) **506**, 343 (2014).

[8] O. A. Hurricane, D. A. Callahan, D. T. Casey, E. L. Dewald, T. R. Dittrich, T. Döppner, S. W. Haan, D. E. Hinkel, L. F. Berzak Hopkins, O. Jones, A. L. Kritcher, S. Le Pape, T. Ma, A. G. MacPhee, J. L. Milovich, J. Moody, A. Pak, H. S. Park, P. K. Patel, J. E. Ralph *et al.*, Inertially confined fusion plasmas dominated by alpha-particle self-heating, Nat. Phys. **12**, 800 (2016).

[9] R. Betti and O. A. Hurricane, Inertial-confinement fusion with lasers, Nature (London) **12**, 435 (2016).

[10] J. Freeman, M. Clauser, and S. Thompson, Rayleigh-Taylor instabilities in inertial-confinement fusion targets, Nucl. Fusion **17**, 223 (1977).

[11] R. D. Richtmyer, Taylor instability in shock acceleration of compressible fluids, Commun. Pure Appl. Math. **13**, 297 (1960).

[12] E. E. Meshkov, Instability of the interface of two gases accelerated by a shock wave, Fluid Dyn. **4**, 101 (1969).

[13] Q. Yang, J. Chang, and W. Bao, Richtmyer-Meshkov instability induced mixing enhancement in the scramjet combustor with a central strut, Adv. Mech. Eng. **6**, 614189 (2014).

[14] E. Muller, B. Fryxell, and D. Arnett, Instability and clumping in SN1987A, Astron. Astrophys. **251**, 505 (1991).

[15] K. Kifonidis, T. Plewa, H. T. Janka, and E. Muller, Non-spherical core collapse supernovae—I. Neutrino-driven convection, Rayleigh-Taylor instabilities, and the formation and propagation of metal clumps, Astron. Astrophys. **408**, 621 (2003).

[16] U. Hwang *et al.*, A million second *Chandra* view of Cassiopeia A, Astrophys. J. **615**, L117 (2004).

[17] K. Kifonidis, T. Plewa, L. Scheck, H. T. Janka, and E. Müller, Non-spherical core collapse supernovae II. The late-time evolution of globally anisotropic neutrino-driven explosions and their implications for SN 1987 A, Astron. Astrophys. **453**, 661 (2006).

[18] E. P. Hicks, Rayleigh-Taylor unstable flames— fast or faster? Astrophys. J. **803**, 72 (2015).

[19] A. Petchenko, V. Bychkov, V. Akkerman, and L.-E. Eriksson, Violent folding of a flame front in a flame-acoustic resonance, Phys. Rev. Lett. **97**, 164501 (2006).

[20] M. Chertkov, V. Lebedev, and N. Vladimirova, Reactive Rayleigh-Taylor turbulence, J. Fluid Mech. **633**, 1 (2009).

[21] A. M. Khokhlov, E. S. Oran, A. Y. Chtchelkanova, and J. C. Wheeler, Interaction of a shock with a sinusoidally perturbed flame, Combust. Flame **117**, 99 (1999).
[22] L. Massa and P. Jha, Linear analysis of the Richtmyer-Meshkov instability in shock-flame interactions, Phys. Fluids **24**, 056101 (2012).
[23] X. Chen, G. Dong, and H. Jiang, A three-dimensional numerical study on instability of sinusoidal flame induced by multiple shock waves, Acta Mech. Sin. **33**, 316 (2017).
[24] Y. Zhou, Rayleigh-Taylor and Richtmyer-Meshkov instability induced flow, turbulence, and mixing. I, Phys. Rep. **720–722**, 1 (2017).
[25] Y. Zhou, Rayleigh-Taylor and Richtmyer-Meshkov instability induced flow, turbulence, and mixing. II, Phys. Rep. **723–725**, 1 (2017).
[26] Y. Zhou, T. T. Clark, D. Clark, S. G. Glendinning, M. A. Skinner, C. M. Huntington, O. A. Hurricane, A. M. Dimits, and B. A. Remington, Turbulent mixing and transition criteria of flows induced by hydrodynamic instabilities, Phys. Plasmas **26**, 080901 (2019).
[27] Y. Zhou, R. J. R. Williams, P. Ramaprabhu, M. Groom, B. Thornber, A. Hillier, W. Mostert, B. Rollin, S. Balachanda, P. H. Powell, A. Mahalov, and N. Attal, Rayleigh-Taylor and Richtmyer-Meshkov instabilities: A journey through scales, Physica D **423**, 132838 (2021).
[28] G. I. Bell, Taylor instability on cylinders and spheres in the small amplitude approximation, Los Alamos National Laboratory Technical Report LA-1321, Los Alamos National Laboratory, US, 1951.
[29] M. S. Plesset, On the stability of fluid flows with spherical symmetry, J. Appl. Phys. **25**, 96 (1954).
[30] R. Epstein, On the Bell-Plesset effects: The effects of uniform compression and geometrical convergence on the classical Rayleigh-Taylor instability, Phys. Plasmas **11**, 5114 (2004).
[31] M. El Rafei, M. Flaig, D. L. Youngs, and B. Thornber, Three-dimensional simulations of turbulent mixing in spherical implosions, Phys. Fluids **31**, 114101 (2019).
[32] D. L. Youngs and B. Thornber, Early time modifications to the buoyancy-drag model for Richtmyer-Meshkov mixing, J. Fluids Eng. **142**, 121107 (2020).
[33] D. L. Youngs and B. Thornber, Buoyancy-drag modelling of bubble and spike distances for single-shock Richtmyer-Meshkov mixing, Physica D **410**, 132517 (2020).
[34] M. El Rafei and B. Thornber, Numerical study and buoyancy-drag modeling of bubble and spike distances in three-dimensional spherical implosions, Phys. Fluids **32**, 124107 (2020).
[35] G. Dimonte, A modal wave-packet model for the multi-mode Richtmyer-Meshkov instability, Phys. Fluids **33**, 014108 (2021).
[36] B. Akula and D. Ranjan, Dynamics of buoyancy-driven flows at moderately high Atwood numbers, J. Fluid Mech. **795**, 313 (2016).
[37] Y. Tian, F. A. Jaberi, Z. Li, and D. Livescu, Numerical study of variable density turbulence interaction with a normal shock wave, J. Fluid Mech. **829**, 551 (2017).
[38] I. Gat, G. Matheou, D. Chung, and P. E. Dimotakis, Incompressible variable-density turbulence in an external acceleration field, J. Fluid Mech. **827**, 506 (2017).
[39] M. L. Wong, D. Livescu, and S. K. Lele, High-resolution Navier-Stokes simulations of Richtmyer-Meshkov instability with reshock, Phys. Rev. Fluids **4**, 104609 (2019).
[40] D. Aslangil, D. Livescu, and A. Banerjee, Effects of Atwood and Reynolds numbers on the evolution of buoyancy-driven homogeneous variable-density turbulence, J. Fluid Mech. **895**, A12 (2020).
[41] A. Banerjee, W. N. Kraft, and M. J. Andrews, Detailed measurements of a statistically steady Rayleigh-Taylor mixing layer from small to high Atwood numbers, J. Fluid Mech. **659**, 127 (2010).
[42] O. Schilling, Progress on understanding Rayleigh-Taylor flow and mixing using synergy between simulation, modeling, and experiment, J. Fluids Eng. **142**, 120802 (2020).
[43] A. Banerjee, Rayleigh-Taylor instability: A status review of experimental designs and measurement diagnostics, J. Fluids Eng. **142**, 120801 (2020).
[44] D. Livescu, Turbulence with large thermal and compositional density variations, Annu. Rev. Fluid Mech. **52**, 309 (2020).
[45] M. L. Wong, J. R. Baltzer, D. Livescu, and S. K. Lele, Analysis of second moments and their budgets for Richtmyer-Meshkov instability and variable-density turbulence induced by reshock, Phys. Rev. Fluids **7**, 044602 (2022).

[46] D. C. Wilcox, *Turbulence Modelling for CFD*, 1st ed. (DCW Industries, 1994).
[47] M. Wolfshtein, Length-scale-of-turbulence equation, Isr. J. Technol. **8**, 87 (1970).
[48] G. Dimonte and R. Tipton, *K-L* turbulence model for the self-similar growth of the Rayleigh-Taylor and Richtmyer-Meshkov instabilities, Phys. Fluids **18**, 085101 (2006).
[49] C. G. Speziale, Analytical methods for the development of Reynolds stress closures in turbulence, Annu. Rev. Fluid Mech. **23**, 107 (1991).
[50] E. Scannapieco and M. Bruggen, Subgrid modeling of AGN-driven turbulence in galaxy clusters, Astrophys. J. **686**, 927 (2008).
[51] O. A. Hurricane, V. A. Smalyuk, K. Raman, O. Schilling, J. F. Hansen, G. Langstaff, D. Martinez, H. S. Park, B. A. Remington, H. F. Robey, J. A. Greenough, R. Wallace, C. A. Di Stefano, R. P. Drake, D. Marion, C. M. Krauland, and C. C. Kuranz, Validation of a turbulent Kelvin-Helmholtz shear layer model using a high-energy-density OMEGA laser experiment, Phys. Rev. Lett. **109**, 155004 (2012).
[52] Y. V. Yanilkin, V. V. Nikiforov, Y. A. Bondarenko, E. V. Gubkov, G. V. Zharova, V. P. Statsenko, and V. I. Tarasov, Two-parameter model and method for computations of turbulent mixing in 2D compressible flows, in *Proceedings of the Fifth International Workshop on the Physics of Compressible Turbulent Mixing, Stony Brook, NY* (World Scientific, Singapore, 1995).
[53] M. Yang, L. L. Wang, and S. D. Zhang, Numerical simulation of turbulent mixing induced by Rayleigh-Taylor instability, Eng. Mech. **28**, 236 (2011).
[54] Y. Zhou, G. B. Zimmerman, and E. W. Burke, Formulation of a two-scale transport scheme for the turbulent mix induced by Rayleigh-Taylor and Richtmyer-Meshkov instabilities, Phys. Rev. E **65**, 056303 (2002).
[55] D. Besnard, F. H. Harlow, R. M. Rauenzahn, and C. Zemach, Turbulence transport equations for variable-density turbulence and their relationship to two-field models, Los Alamos National Laboratory Report LA-12303-MS, Los Alamos National Laboratory, US, 1992.
[56] J. D. Schwarzkopf, D. Livescu, R. A. Gore, R. M. Rauenzahn, and J. R. Ristorcelli, Application of a second-moment closure model to mixing processes involving multicomponent miscible fluids, J. Turbul. **49**, 1 (2011).
[57] J. D. Schwarzkopf, D. Livescu, J. R. Baltzer, R. A. Gore, and J. R. Ristorcelli, A two-length scale turbulence model for single-phase multi-fluid mixing, Flow, Turbul. Combust. **96**, 1 (2016).
[58] O. Schilling, Self-similar Reynolds-averaged mechanical-scalar turbulence models for Rayleigh-Taylor, Richtmyer-Meshkov, and Kelvin-Helmholtz instability-induced mixing in the small Atwood number limit, Phys. Fluids **33**, 085129 (2021).
[59] F. S. Pereira, F. F. Grinstein, D. M. Israel, R. Rauenzahn, and S. S. Girimaji, Partially averaged Navier-Stokes closure modeling for variable-density turbulent flow, Phys. Rev. Fluids **6**, 084602 (2021).
[60] B. J. Balakumar, G. C. Orlicz, J. R. Ristorcelli, S. Balasubramanian, K. P. Prestridge, and C. D. Tomkins, Experimental study of initial condition dependence on turbulent mixing in shock-accelerated Richtmyer-Meshkov fluid layers, J. Turbul. **14**, 1170 (2013).
[61] G. C. Orlicz, S. Balasubramanian, and K. P. Prestridge, Incident shock Mach number effects on Richtmyer-Meshkov mixing in a heavy gas layer, Phys. Fluids **25**, 114101 (2013).
[62] C. D. Tomkins, B. J. Balakumar, G. C. Orlicz, K. P. Prestridge, and J. R. Ristorcelli, Evolution of the density self-correlation in developing Richtmyer-Meshkov turbulence, J. Fluid Mech. **735**, 288 (2013).
[63] C. R. Weber, N. S. Haehn, J. G. Oakley, D. A. Rothamer, and R. Bonazza, An experimental investigation of the turbulent mixing transition in the Richtmyer-Meshkov instability, J. Fluid Mech. **748**, 457 (2014).
[64] V. K. Tritschler, B. J. Olson, S. Lele, S. Kand Hickel, X. Y. Hu, and N. A. Adams, On the Richtmyer-Meshkov instability evolving from a deterministic multimode planar interface, J. Fluid Mech. **755**, 429 (2014).
[65] M. Mohaghar, J. Carter, G. Pathikonda, and D. Ranjan, The transition to turbulence in shock-driven mixing: Effects of mach number and initial conditions, J. Fluid Mech. **871**, 595 (2019).
[66] D. Livescu, J. R. Ristorcelli, R. A. Gore, S. H. Dean, W. H. Cabot, and A. W. Cook, High-Reynolds number Rayleigh-Taylor turbulence, J. Turbul. **10**, N13 (2009).
[67] M. Lombardini, D. I. Pullin, and D. I. Meiron, Turbulent mixing driven by spherical implosions. Part 2. Turbulence statistics, J. Fluid Mech. **748**, 113 (2014).

[68] B. E. Morgan, B. J. Olson, W. J. Black, and J. A. McFarland, Large-eddy simulation and Reynolds-averaged Navier-Stokes modeling of a reacting Rayleigh-Taylor mixing layer in a spherical geometry, Phys. Rev. E **98**, 033111 (2018).

[69] I. Boureima, P. Ramaprabhu, and N. Attal, Properties of the turbulent mixing layer in a spherical implosion, J. Fluids Eng. **140**, 050905 (2018).

[70] B. Thornber, J. Griffond, P. Bigdelou, I. Boureima, P. Ramaprabhu, O. Schilling, and R. J. R. Williams, Turbulent transport and mixing in the multimode narrowband Richtmyer-Meshkov instability, Phys. Fluids **31**, 096105 (2019).

[71] X. Li, Y. Fu, C. Yu, and L. Li, Statistical characteristics of turbulent mixing in spherical and cylindrical converging Richtmyer-Meshkov instabilities, J. Fluid Mech. **928**, A10 (2021).

[72] A. Garcia-Uceda Juarez, A. Raimo, E. Shapiro, and B. Thornber, Steady turbulent flow computations using a low mach fully compressible scheme, AIAA J. **52**, 2559 (2014).

[73] M. El Rafei and B. Thornber, A comparison of a modified curvilinear approach for compressible problems in spherical geometry and a truly spherical high-order method, in *Proceedings of the 21st Australasian Fluid Mechanics Conference* (AFMC, Adelaide, Australia, 2018).

[74] C. S. Kim, C. Kim, and O. H. Rho, Parallel computations of high-lift airfoil flows using two-equation turbulence models, AIAA J. **38**, 1360 (2000).

[75] S. Gottlieb and C. W. Shu, Total variation diminishing Runge-Kutta schemes, Math. Comput. **67**, 73 (1998).

[76] R. J. Spiteri and S. J. Ruuth, A class of optimal high-order strong-stability preserving time discretization methods, SIAM J. Numer. Anal. **40**, 469 (2002).

[77] B. Thornber, A. Mosedale, D. Drikakis, D. Youngs, and R. Williams, An improved reconstruction method for compressible flows with low Mach number features, J. Comput. Phys. **227**, 4873 (2008).

[78] B. Thornber, D. Drikakis, D. L. Youngs, and R. J. R. Williams, The influence of initial conditions on turbulent mixing due to Richtmyer-Meshkov instability, J. Fluid Mech. **654**, 99 (2010).

[79] B. Thornber and Y. Zhou, Energy transfer in the Richtmyer-Meshkov instability, Phys. Rev. E **86**, 056302 (2012).

[80] M. Groom and B. Thornber, Direct numerical simulation of the multimode narrowband Richtmyer-Meshkov instability, Comput. Fluids **194**, 104309 (2019).

[81] M. Groom and B. Thornber, The influence of initial perturbation power spectra on the growth of a turbulent mixing layer induced by Richtmyer-Meshkov instability, Physica D **407**, 132463 (2020).

[82] M. Groom and B. Thornber, Reynolds number dependence of turbulence induced by the Richtmyer-Meshkov instability using direct numerical simulations, J. Fluid Mech. **908**, A31 (2021).

[83] M. Groom and B. Thornber, Numerical simulation of an idealised Richtmyer-Meshkov instability shock tube experiment, J. Fluid Mech. **964**, A21 (2023).

[84] D. Livescu and J. R. Ristorcelli, Variable-density mixing in buoyancy-driven turbulence, J. Fluid Mech. **605**, 145 (2008).

[85] B. Thornber, Impact of domain size and statistical errors in simulations of homogeneous decaying turbulence and the Richtmyer-Meshkov instability, Phys. Fluids **28**, 045106 (2016).

[86] M. Flaig, D. L. Youngs, D. Clark, C. Weber, and B. Thornber, Single-mode perturbation growth in an idealized inertial confinement fusion implosion, J. Comput. Phys. **371**, 801 (2018).

[87] C. C. Joggerst, A. Nelson, P. Woodward, C. Lovekin, T. Masser, C. L. Fryer, P. Ramaprabhu, M. Francois, and G. Rockefeller, Cross-code comparisons of mixing during the implosion of dense cylindrical and spherical shells, J. Comput. Phys. **275**, 154 (2014).

[88] D. L. Youngs and R. J. R. Williams, Turbulent mixing in spherical implosions, Int. J. Numer. Methods Fluids **56**, 1597 (2008).

[89] Y. Yang, Q. Zhang, and D. H. Sharp, Small amplitude theory of Richtmyer-Meshkov instability, Phys. Fluids **6**, 1856 (1994).

[90] D. L. Youngs, Effect of initial conditions on self-similar turbulent mixing, in *Proceedings of the Ninth International Workshop on the Physics of Compressible Turbulent Mixing* (IWPCTM, Cambridge, UK, 2004).

[91] D. L. Youngs, Numerical simulation of turbulent mixing by Rayleigh-Taylor instability, Physica D **12**, 32 (1984).
[92] L. Skrbek and S. R. Stalp, On the decay of homogeneous isotropic turbulence, Phys. Fluids **12**, 1997 (2000).
[93] V. Mons, J. Chassaing, T. Gomez, and P. Sagaut, Is isotropic turbulence decay governed by asymptotic behavior of large scales? An eddy-damped quasi-normal Markovian-based data assimilation study, Phys. Fluids **26**, 115105 (2014).
[94] Y. Zhou, W. H. Cabot, and B. Thornber, Asymptotic behavior of the mixed mass in Rayleigh-Taylor and Richtmyer-Meshkov instability induced flows, Phys. Plasmas **23**, 052712 (2016).
[95] D. L. Youngs, Numerical simulation of mixing by Rayleigh-Taylor and Richtmyer-Meshkov instabilities, Laser Part. Beams **12**, 725 (1994).
[96] D. Livescu and J. R. Ristorcelli, Buoyancy-driven variable-density turbulence, J. Fluid Mech. **591**, 43 (2007).
[97] P. Ramaprabhu, G. Dimonte, and M. J. Andrews, A numerical study of the influence of initial perturbations on the turbulent Rayleigh-Taylor instability, J. Fluid Mech. **536**, 285 (2005).
[98] A. Banerjee and M. J. Andrews, 3D simulations to investigate initial condition effects on the growth of Rayleigh-Taylor mixing, Int. J. Heat Mass Transf. **52**, 3906 (2009), special issue honoring Professor D. Brian Spalding.
[99] D. Aslangil, A. Banerjee, and A. G. W. Lawrie, Numerical investigation of initial condition effects on Rayleigh-Taylor instability with acceleration reversals, Phys. Rev. E **94**, 053114 (2016).